Seismic, geochemical and sedimentological characteristics of storm deposits from the Durban continental shelf, South Africa

by

Shannon Louise Dixon (BSc Hons)

College of Agriculture, Engineering and Science,

School of Agriculture, Earth and Environment Sciences,

Discipline of Geological Sciences

December 2015

Submitted in fulfilment of the academic requirements for the degree of Master of Science in the School of Agriculture, Earth and Environmental Sciences, University of KwaZulu-Natal, Westville.

As the candidate's supervisor I have approved this thesis/dissertation for submission.

Signed:..…….…… Name: ……..…..…… Date: ..……

Abstract

The Durban shelf is a wave-dominated, high energy setting, characterised by submerged shorelines at depths of ~60 m, backed to landward by low-relief backbarrier depressions. The exposure at the seafloor of a back-barrier/lagoon complex, coupled with the general high wave energy of the shelf makes for a unique opportunity to examine records of marine storminess, preserved as tempestites in the shelf stratigraphy. This thesis examined a variety of ultra-high resolution seismic data, coupled with multibeam bathymetry, core and sedimentological data. High resolution XRF, XRD and other provenance proxies were also examined in order to reveal cycles of storminess that have impacted the lower shoreface offshore Durban. These are integrated with a rigorous geochronological framework. The seismic sections revealed two distinct packages which comprise the unconsolidated shoreface (Unit A and B). These are further subdivided into an upper five packages (Sub-unit B1-B5 and sub-unit A-Ai). Cores that penetrated this sediment enabled a further correlation with that of the bounding surfaces, sediment compositions and the nature of individual sub units.

Unit A and Ai are considered incised valley fills corresponding to organic-rich fine sand of the central basin and flood tide delta deposits with a distinctly higher terrigenous sediment signature in comparison to the overlying sediment packages. The tidal ravinement surface (tRS) is restricted to the incised valley where it separates unit A and Ai. The wave ravinement surface (WRS) truncates the incised valley fills and is overlain by unconsolidated material of unit B. Sub-units B3 and B4 are storm associated deposits which are of particular interest to this study.

Sub-unit B3 comprises a number of high energy deposits, namely mudballs; these deposits consist of organic rich material indicative of storm winnowing of an exposed muddy backbarrier (such as presently occurring along sectors of the adjoining coastal plain). This is corroborated by the geochemical analyses of the mudballs which displays significantly higher concentrations of terrigenous elements (Si, Al, K, Ti and Rb), in comparison to the surrounding sediment, indicative of a terrigenous sediment origin. The centre of the mudball was dated at 9 850 ± 50 cal yrs BP. The outer veneer dates to 3 835 ± 35 cal yrs BP and represents the final phase of deposition in the lower shoreface. The mudballs are encased in coarse sediment, dominated by Ca and Sr

elemental concentrations, suggestive of a marine origin. Sub-unit B4 consists of alternating horizons of storm generated gravel horizons displaying increased marine elemental signatures, interbedded with finer sediment with increased terrigenous concentrations indicative of fair-weather conditions.

It was found that horizons of coarser material had higher elemental signatures of Ca and Sr indicating a predominantly marine input into the system. These horizons are intercalated with finer material with distinctly higher concentrations of elements associated with terrigenous source material that represents fair-weather suspension settling of terrestrial materials.

Based on modelling of the largest experienced contemporary marine storm (Hs = 8.5 m), it is clear that storm waves do not significantly rework gravelly sediment on the lower shoreface, especially in the areas of smooth seafloor where the cores are situated. Bathymetry of the area shows no contemporary evidence for storm scour or gravel deposition. As the palaeo-tempestites date to a time when sea level occupied a similar position to that of today, it is logical to assume these represent much larger storm events than are commonly experienced.

This study shows for the first time a period of increased storminess in the Indian Ocean between 6 480 ± 40 cal yr BP to 4 595 ± 35 cal yr BP; a time linked to a strongly positive Indian Ocean Dipole (IOD) anomaly and increased sea surface temperatures (SST). With further global warming, it appears that Durban may be more vulnerable to large marine storms as the associated changes in atmospheric circulation patterns and oceanic currents promote the formation of positive IOD phenomena.

COLLEGE OF AGRICULTURE, ENGINEERING AND SCIENCE

DECLARATION 1 – PLAGIARISM

I _____ declare that

1. The research reported in this thesis, except where otherwise indicated, is my original research.

2. This thesis has not been submitted for any degree or examination at any other university.

3. This thesis does not contain other persons' data, pictures, graphs or other information, unless specifically acknowledged as being sourced from other persons.

4. This thesis does not contain other persons' writing, unless specifically acknowledged as being sourced from other researchers. Where other written sources have been quoted, then:

a. Their words have been re-written but the general information attributed to them has been referenced

b. Where their exact words have been used, then their writing has been placed in italics and inside quotation marks, and referenced.

5. This thesis does not contain text, graphics or tables copied and pasted from the Internet, unless specifically acknowledged, and the source being detailed in the thesis and in the References sections.

Signed:_____.

CMC Feb 2012

Form EX1-5

TABLE OF CONTENTS

Abstract i
Declaration iii
List of Figures vi
List of Tables viii
Acknowledgements x

CHAPTER 1

1.1. Introduction 1
1.2. Research aims and objectives 2
1.3. Marine storms and shoreface evolution 4
1.3.1. Shoreline storm deposits 4
1.3.1.1. Preservation potential of storms deposits and sea level 5
1.3.2. Storm deposits on the continental shelf 7

CHAPTER 2

2.1. Regional setting 8
2.2. Oceanography and climate 9
2.3. Geological setting 10
2.4. Sea-level changes 11

CHAPTER 3

3.1. Methods and Materials 13
3.1.1. Ultra-high resolution seismic profiling 13
3.1.2. Coring 13
3.1.3. Multibeam bathymetry 14
3.1.4. Grain size analysis 14
3.1.5. Geochemical and mineralogical analyses 15
3.1.5.1. Bulk geochemistry (XRD) 15
3.1.5.2. Elemental Analysis (XRF) 16
3.1.6. Storm wave modelling 16

CHAPTER 4

4.1. Results 18

4.1.1. Seismic stratigraphy 18
4.1.2. Core lithology 21
4.1.2.1. Facies successions 21
4.1.2.2. Grain size 22
4.1.3. Elemental chemistry 23
4.1.3.1. Down-core distribution 24
4.1.3.2. Correlation with grain size and XRF 25
4.1.3.3. XRD 26
4.1.4. Chronostratigraphy 29
4.1.5. Bathymetry and wave modelling 31
CHAPTER 5
5.1. Discussion 34
5.1.1. Seismic and lithostratigraphic interpretations 34
5.1.2. The significance of Sub-unit B3 and B4 37
5.1.3. Timing of storm induced events 38
5.1.4. Comparison with contemporary conditions 39
CHAPTER 6
6.1. Conclusion 41
References 43
Appendix I 61
Appendix II 72

List of Figures page

Figure 1. Locality map of the study area, located offshore the central KwaZulu-Natal continental shelf, on the east coast of South Africa. Important to note here is the ~200 km2 sun shaded bathymetry located offshore of Durban (data provided by eThekweni Municipality and presented in Green et al., 2013b). The solid lines indicate the position of the PARASOUND seismic reflection profiles (Figure 4a, 4b and 4c) and the core locations.....3

Figure 2. Mid-Pleistocene to Holocene sea level curve for the east coast of South Africa modified after Ramsay and Cooper (2002). Note that the time period of interest spans the period 13 000 yrs BP to the late Holocene. Dates obtained from core material are plotted relative to the sea level curves for both cores GeoB18303-2 and GeoB18304-1. 12

Figure 3. Holocene sea level curve for the East Coast of South Africa modified after Ramsay (1995). Sea-level reached its current position ca. 6.5 ka BP with a maximum highstand of +3.5 m above present sea level followed by subsequent sea-level fluctuations of ~1-2 m. 12

Figure 4. Shore-perpendicular seismic profiles (locations are depicted in figure 1). Aeolianite/beachrock ridges are shown as yellow. Note the covering of Unit B in all sections. a) Unit A infills the topography formed in the subaerial u/c. Unit B1 is restricted to the transition to the outer shelf. Unit B2 and unit B3 onlap the seaward edge of the aeolianites/beachrock ridges. b). Unit B3 occurs as isolated reflector packages with a more chaotic internal reflector configuration than Unit B2. Unit B4 is restricted to depths of 30-40 m and occurs as isolated packages truncated by surface. c) Unit B5 marks the uppermost layers in the inner shelf regions. 20

Figure 5. Graphic logs of cores GeoB18304-1 and GeoB18303-2 with associated sedimentary facies. Note the location of the core relative to the seismic units B5, B4 and unit Ai in core GeoB18304-1 and unit B3 and units Ai and and A in core GeoB18303-2. The lower margin of unit B4 consists of alternating shell hash horizons interbedded with finer sediment. Facies 3 contains dated organic rich mudballs encased in coarse shelly

sediment. Dates obtained and surfaces intersected are indicated along the depth profile of the sedimentary logs. 22

Figure 6. Sedimentology, grain size, elemental chemistry and mineralogy of core GeoB18303-2. All depths are relative to the collar of the core. a) Grain size data for both the bulk and terrigenous sediment fractions measured in phi (Ø). b) Down-core XRF elemental chemistry. Note the strong correlations of elements below 1.45 m depth. Also note the strong terrigenous elemental signatures from depths characterised by mud balls. c) XRD Mineral concentrations. 27

Figure 7. Sedimentology, grain size, elemental chemistry and mineralogy of core GeoB18304-1. All depths are relative to the collar of the core. a) Grain size data for both the bulk and terrigenous sediment fractions measured in phi (Ø). Note the inverse relationship between the bulk and terrigenous sediment is present below depths of 3.15 m. b) Down-core XRF elemental chemistry. Note the strong correlation of elements at depths below 3.15 m. c) XRD Mineral concentrations 28

Figure 8. Multibeam bathymetry of the study area. Note the two discreet seafloor types marked by rugged seafloor relief and smooth featureless seafloor relief. The high relief areas represent outcrop of beachrock/aeolianites, whereas the low relief areas are marked by unconsolidated sediment. Isolated mounds of unconsolidated sediment occur sporadically at depths of between 40 m and 60 m. Upper left image displays a portion of the seafloor bathymetry in further detail, the bathymetric lows are of particular interest as they are associated with sediment accumulation on the sea floor. 32

Figure 9. A regular structured grid with 5 meters depth resolution was used for representing the computational domain. a) The bathymetric grid representing the bottom conditions of the study area. b) Displays the modelled wave field near bottom orbital velocities, represented according to the threshold value for gravelly sediment mobility greater than 0.52 m/s for offshore boundary conditions for the March 2007 storm event (Hs- 8.5 m; Hmax-12.38 m; Tp- 16.6sec; θ- 147°). The line present represents the position of the old incised valley after Green et al (2013b). 33

List of Tables page

Table 1. Seismic stratigraphic observations and interpretations off the Durban continental shelf in central KwaZulu-Natal. Seismic units are defined as Unit A and Unit B which are further sub divided based on internal configurations. Descriptions of these units are provided which include the underlying surface, seismic characteristics, spatial distribution and cross sectional thickness of individual units. Based on these observations the environment of deposition is then inferred.....19

Table 2. Chronostratigraphy of GeoB18304-1 and GeoB18303-2. AMS radiocarbon dates are indicated, together with the composition of material dated, interpretation of the intersected unit/bracketing surface and the associated sedimentary facies 30

Table 3. Quantitative XRF data for Core GeoB18304-1, all values are displayed as weight percentage (wt%) at 5 cm intervals with depth down core. It should be noted that Ca and Si are interchangeable the most abundant elements present 61

Table 4. Quantitative XRF data for Core GeoB18303-2, all values are displayed as weight percentage (wt%) at 5 cm intervals with depth down core. It should be noted that Ca and Si are interchangeable the most abundant elements present 65

Table 5. Quantitative XRD data for Core GeoB18304-1, a total of 14 samples were from horizons indicated with depth down core. All values are displayed as weight percentage (wt%). It should be noted that Quartz (Qtz) and Carbonate mineral concentration are the most abundant elements present in the distal core. 70

Table 6. Quantitative XRD data for Core GeoB18303-2, where a total of 7 samples were taken from selected horizons with depths indicated. All values are displayed as weight percentage (wt%). It should be noted that Quartz (Qtz) and Carbonate mineral concentration are the most abundant elements present in the proximal core. 71

Table 7. Grainsize data for core GeoB18304-1 sampled at 5 cm depth intervals. All grain size values for both the clastic and bulk sediment component are displayed as phi values. In comparison with the bulk sediment component it is evident that the clastic sediment is significantly finer with higher phi values displayed.....72

Table 8. Grainsize data for core GeoB18303-2 sampled at 5 cm depth intervals. All grain size values for both the clastic and bulk sediment component are displayed as phi values. In comparison with the bulk sediment component it is evident that the clastic sediment is significantly finer with higher phi values displayed. When compared to core GeoB18304-1 it is evident that the more distal core is composed of coarser material with lower grain size phi values for the clastic and bulk sediment component 75

ACKNOWLEDGEMENTS

Firstly, I would like to thank Prof. Andrew Green for his continued encouragement and emotional support, without you this thesis would not have been possible. Your constant motivation has been a driving factor to make this a successful venture. I appreciate the long hours and faith you have had in me, being part of your marine unit has been an honour and you deserve everything you have worked so hard for. I am so proud of you.

This project forms a sub project of the Regional Archive for Integrated iNvestigations (RAIN). I would like to thank RAIN for providing the opportunity for me to take part on a cruise aboard the RV Meteor, M102. I was fortunate enough to collect the majority of my data over the duration of this cruise. Without these data this project would never have been possible. I would like to acknowledge the captain and crew of the RV Meteor for their dedication in very rough sea conditions. I would also like to thank the German Academic Exchange Service (DAAD) for providing the funds and the opportunity to perform the geochemical analyses at the University of Bremen, under the supervision of the very talented Dr. Matthias Zabel (the head of the marine geochemistry unit at the University of Bremen), and his amazing team. I would especially like to thank a special German lady, Dr. Annette Hahn, for introducing me to German culture, ensuring I was constantly busy in the labs and providing the occasional social relief. Sharing an office with you was a pleasure.

I would like to thank Dr. Carlos Loureiro, for his advice and generous help in setting up the SWAN model. I would like to acknowledge Dr. Christoph Voigt from the department of Geoscience/ Crystallography for the x-ray diffraction results and Dr. Jürgen Titschack for supervising the lab work while obtaining grainsize results using the Coulter laser particle sizer at MARUM, University of Bremen.

To my best friend and partner in crime Cameron Pistorius, thank you for your encouragement, I know these last two years have been tough but in the end it was totally worth it. I would like to thank Dr. Errol Wiles for all the long office chats and laughs (you made my eyes water just looking in your direction). My long-time friend Lauren Pretorius for making all those awkward moments bearable and bringing the screaming laughter into the department. To the soon to be Dr. Lauren Hoyer, Jannie Weitz, Talicia

Pillay and Clarice Romer getting to know you over the past two years has been a privilege and the department would be a lonely place without such special people.

Lastly I would like to thank my loving family. They have been positive and supportive throughout this journey and I know it has not been easy, but without you none of this would be possible.

This project was partly funded by the Andrew Geddes Bain Fund of the Geological Society of South Africa, the German Academic Exchange Service (DAAD), a National Research Foundation Innovation Scholarship and a college scholarship from UKZN.

CHAPTER 1

1.1. Introduction

Sedimentary deposits produced by marine storms provide valuable information on the intensity and frequency of marine inundation as a result of such extreme events With increasing interest in marine storms, storm-driven coastal erosion and storm wave deposition in the light of changing climate, there is a need to frame modern observation of marine storm events in light of those experienced previously (Shinn et al., 1993; Liu and Fearn, 1993; 2000; Collins et al., 1999; Donnelly et al., 2001a;b). A significant body of global literature exists concerning palaeo-storminess that is focussed on the introduction of washover material to the backbarrier areas of salt marshes, lagoons and estuaries. The occurrence of coarse marine sediment intercalated within the stratigraphy serves as a proxy for marine storms (Dott and Bourgeois, 1982; Kochel and Dolan, 1986); of which the detailed mapping of the geometry and spatial distribution can allow discrimination between a tsunamigenic or storm wave origin. Little direct evidence of Holocene marine storminess from high-energy shelf records exists. This may due to a low preservation potential due to shoreface modification during contemporary storms (e.g. Backstrom et al., 2009) or due to poor preservation of geochemical proxies as a result of sandy substrate. Most offshore storm records from marine archives tend to focus on the accumulation of muddy material which is subjected to geochemical analyses that act as proxies for the identification of climatic variability (e.g. Schefuß et al., 2011).

The frequency and intensity of Holocene palaeo-storminess is of particular interest to this study. Recent assumptions consider global warming as a driver for increasing storm frequency and intensity. These studies have mainly focussed on relatively recent events (< 5 000 yrs before present) (e.g. Donnelly and Woodruffe, 2007) and there is a relative dearth of attempts to further elucidate the record of storminess for the early to mid-Holocene, especially regarding marine storminess.

Holocene sediment is relatively thinly developed on the east coast of South Africa, with major depocentres usually taking the form of progradational sandy bodies (Martin and

Flemming, 1986) and isolated incised valley fills (e.g Green, 2009a and 2009b). The coupling of the prevailing regional ocean circulation system (Agulhas current), together with the high wave energy precludes the development of substantial muddy depocentres and favours the erosion rather than the accumulation of sediment (e.g. Green et al., 2012a).

This project is specifically concerned with records of storminess that exist on the shelf offshore of Durban (Fig. 1). Here, recent discoveries (Green et al., 2012a; Green et al., 2013b) revealed the presence of thickly developed Holocene sediments that comprise a barrier-back barrier system that was overstepped during the early Holocene (Pretorius et al., 2016). The general evolution of this system from a fluvial to back barrier lagoon has been linked to the Younger-Dryas stillstand (12.7-11.6 Ka BP) (Camoin et al., 2004); a period of cool and dry conditions during a period of sea-level slowstand (Green et al., 2013b). The back barrier thus holds the key to identifying storm frequency and intensity associated from this period to present day. In particular, direct comparisons between storminess associated with a cooler and dryer period, and records reflecting contemporary storminess from the South African coastline (e.g. Salzmann and Green, 2012) can be made.

1.2. Research aims and objectives

The overall aim of this project is to assess the accumulation, distribution and architecture of marine-derived storm deposits preserved in an overstepped lagoon complex on the Durban shelf.

The following questions are assessed within this study. These include:

1. What form do these storm deposits take and what are their chronologies?
2. To what degree have storms influenced the South African coastline since 12 000 years before present to the late Holocene?
3. Can these be strictly related to change in climate, or is sea-level fluctuation also a factor?

The following objectives should be met to achieve this aim:

1. To map the geometry of storm deposits using seismic means in order to determine the nature and timing of these events?
2. To examine their sedimentological and geochemical characteristics.
3. To determine whether these are washover deposits into the back barrier areas of this system or do they represent tempestites?
4. To determine the frequency of extreme wave influence on the shelf.
5. To further the framework of palaeo-extreme wave records by extending these into the mid-Holocene or earlier depending on the material cored.

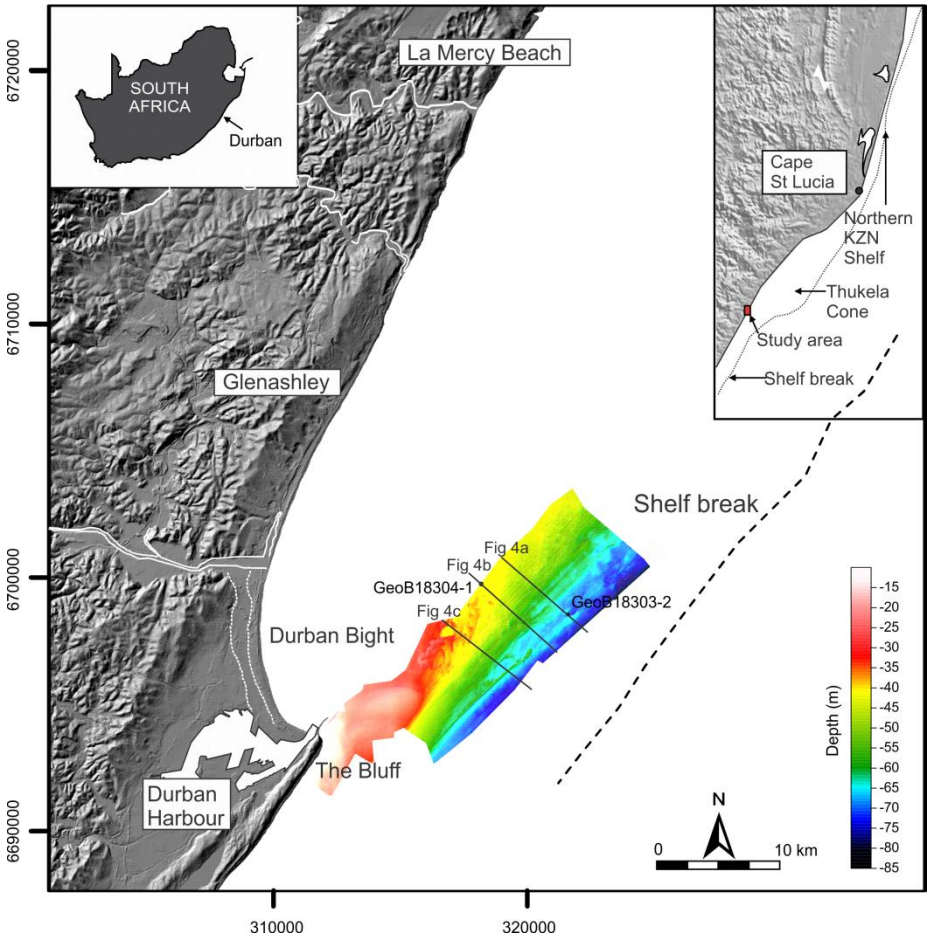

Figure 1. Locality map of the study area, located offshore the central KwaZulu-Natal continental shelf, on the east coast of South Africa. Important to note here is the ~200 km2 sun shaded bathymetry located offshore of Durban (data provided by eTthekweni Municipality and presented in Green et al., 2013b). The solid lines indicate the position of the PARASOUND seismic reflection profiles (Figure 4a, 4b and 4c) and the core locations.

1.3. Marine storms and shoreface evolution

Coastal evolution is an ongoing process resulting in continuous modification and destruction of sedimentary and stratigraphic evidence (Kraft and Chrzastowsk, 1978). High energy coastal processes are considered responsible for the modification and evolution of the shoreface system, the key area which this study will focus on. In particular, storm beds located on the continental shelf show the complex interaction between waves, topography, meteorology and sediment availability (e.g. Keen et al., 2012). Masselink and van Heteren (2014) indicate the need to understand the coupled impact of meteorological and oceanographic conditions in the oceans when investigating coastal impacts of storms. Depending on their relative intensities, the tidal and atmospheric conditions (i.e. storm surge and increased wave run-up), and the depth of area studied, storm deposits may take the form of either shoreline, upper shoreface, or lower shoreface hosted features.

1.3.1. Shoreline storm deposits

Barriers commonly form above high tide and are mostly wave-constructed coastal features (Kraft and Chrzastowsk, 1978). Back barrier environments have become the focal area for the study of storm deposits (Delaney and Devoy, 1995; Ehlers et al., 1993; Guillen et al., 1994; Leatherman and Williams, 1977; Liu and Fearn, 1993; Morton, 1979), as barriers are typically separated from the mainland either by a lagoon or estuary (Kraft and Chrzastowsk, 1978). Storm surges associated with high energy events result in a landwards migration of shoaling waves which overtop the barrier resulting in enhanced over wash during storms (Zong and Tooley, 1999; Forbes et al., 2004). Deposits associated with these high energy events are present as interbedded mud and sand, and are commonly referred to as washover or washover fans (Leatherman, 1977). These deposits can be generated by high energy marine conditions including tsunamis and storms, with comparable depositional characteristics and internal sedimentary structures making it very difficult to differentiate between these deposits in the sedimentary record (Nanayama et al., 2000; Goff et al., 2004; Tuttle et

al., 2004; Kortekaas and Dawson, 2007; Morton et al., 2007; Komatsubara et al., 2008; Switzer and Jones, 2008a; Phantuwongraj and Choowong, 2012).

Washover deposits were described in the 1960's and 1970's by a number of authors from both modern (c.f. Psuty, 1965; Stapor, 1971; Oertel, 1975; Schwartz, 1975) and ancient (c.f. Berg and Davies, 1968; Davies et al., 1971) environments. They primarily consist of 'horizontally bedded, alternating layers of terrigenous sand, shell fragments, and heavy minerals that reflect changing hydraulic competence and tidal variations during storm surge' (Kochel and Dolan, 1986). Along rocky coast lines storm deposits are preserved as storm swash terrace's (McKenna et al., 2012; Dixon et al., 2015), these deposits occur adjacent to laterally extensive shore platforms and/or boulder beaches with sufficient accommodation space at the rear of the shore platform. They form as seaward dipping coast parallel, seaward thinning sediment wedges (McKenna et al., 2012; Dixon et al., 2015). Storm swash terrace's are composed of interbedded high energy marine storm deposits, preserved in the stratigraphy as horizons composed of marine derived sand and gravel beds with occasional boulders and shell hash horizons; these are interlayered with organic rich terrestrial sand and silt deposited during intervals between storms.

1.3.1.1. Preservation of storm deposits and sea level

The preservation potential of storm horizons have been linked to the rate of bioturbation, frequency of overwash, initial thickness of the units, and the magnitude and rate of sea-level change. Ritchie and Penland, (1988) indicated that hydraulic conditions during these high energy events are strongly controlled by barrier elevation, the degree of storm surge, overwash flow constraints and storm wave height. Biological and physical reworking together with storm scour may rework and destroy the underlying overwash deposits (Leatherman and Williams, 1977). High sediment supply together with frequency of overwash events are major factor in determining the amount of reworking of a deposit. Keen et al. (2004) indicated a higher degree of preservation of storm beds in modern environments, associated with limited reworking by burial with sediment derived from fair weather conditions.

The preservation of washover deposits in the sedimentary record has been attributed to the rate and magnitude of sea-level change (Deery and Howard, 1977). Transgressive conditions associated with sea-level rise commonly result in the occurrence of washover deposits, a key transgressive stratigraphic facet. Studies focusing on Holocene barriers located offshore Florida, USA, display evident washover deposits in the stratigraphic record (Davis and Kuhn, 1985; Davis et al., 1989b). The formation and preservation of washover deposits and modern barrier systems is thus of major importance to better understand and interpret the ancient coastal record (Kraft and Chrzastowsk, 1978).

The rate of sea-level rise and sediment availability strongly influences the preservation of washover deposits (Bridges, 1976; Percival, 1992; Willis and Moslow, 1994). Slow rates of sea rise are usually associated with the landward migration of a barrier through rollover (Swift, 1968; Swift et al., 1991; Belknap and Kraft, 1981; Reinson, 1992). When coupled with low sediment availability, reworking of the barrier and shoreline deposits may be complete, resulting in very limited preservation of washover deposits in the offshore stratigraphic profile (Swift and Moslow, 1982; Leatherman et al., 1983; Reinson, 1992). Rapid sea-level rise is associated with barrier overstepping (Curray, 1964; Swift, 1968; Rampino and Sanders, 1980). When coupled with high sediment availability, barrier and shoreline deposits may become stranded offshore with minimal reworking and thus enhanced preservation.

Advances in geophysical techniques and the availability of commercial data has enabled the identification of submerged landscapes and associated coastal sedimentary sequences (possibly including washover) from various depths on the continental shelves (Browne, 1994; Shaw et al., 2009; Kelley et al., 2010; Timmons et al., 2010). It is accepted that transgressive sediments are uncommon on the continental shelf (Storms and Swift, 2003; Mellet et al., 2012; Shaw, 2005), however under conditions of overstepping as described above, they may be preserved.

1.3.2. Storm deposits on the continental shelf

The majority of studies have focused on contemporary storm bed production (Hayes, 1967; Morton, 1981; Snedden et al., 1988; Simms et al., 2007; Keen et al., 2012). These studies show that storm deposits occur as discrete horizons, usually produced by large weather systems (e.g. tropical cyclones) and similarly reflect low recurrence intervals, usually on a dominantly low energy shelf. Preservation potential of these deposits is a function of subsequent storms of lower magnitude, the initial depositional thickness, the long recurrence intervals between events and the rate of burial by significant accumulations of fair weather sediment (Bentley et al., 2002; Keen et al., 2004; 2012).

These storm deposits, commonly termed tempestites, have erosive basal surfaces and are strongly associated with hummocky cross stratification comprising the storm deposited sand unit (Dott and Bourgeois, 1982). The generation of tempestite beds occur in two stages (Aigner and Reineck, 1982; Snedden and Nummedal, 1990), an initial sandy basal layer consistent with the presence of the hummocky cross stratification, followed by the deposition of finer material coinciding with the final stages of a high energy coastal event, forming a mud drape. These are commonly restricted to the lower shoreface environment.

On the upper shoreface, storm horizons can take the form of rippled scour depressions or sorted bedforms; scoured portions of the inner shelf that host gravel and bioclastic-rich debris. These form from the storm-ebb or return flows which are a result of storm-surge piling excess water onto the upper shoreface and surfzone (e.g. Murray and Thieler, 2004; Goff et al., 2005). Their stratigraphic significance is unclear, however the coarse shelly lags have been found to self-reinforce turbulent flows, thus enhancing their persistence in the stratigraphic record (Murray and Thieler, 2004). Rippled scour depressions are typically associated with shoreface connected ridges in the lower shoreface and are considered to act as conduits for sediment supply to the lower shoreface during storminess (Snedden et al., 2011; Green and Smith, 2012).

CHAPTER 2

2.1. Regional setting

This study focuses on the mid-shelf (lower shoreface) of the Durban Bight of KwaZulu-Natal. The Durban Bight comprises a crenulate bay bound to the south by a large headland (The Bluff). There are three main rivers which discharge into the Indian Ocean offshore of Durban. These are (from north to south) the Mdloti, Mhlanga and Mgeni Rivers. The Mgeni River is located nearest to the study area and is the fourth largest river in KwaZulu-Natal to discharge into the Indian Ocean (Badenhorst et al., 1989). Goodlad (1986) subdivided the adjoining continental shelf of eastern South Africa into three physiographic zones, which include a very narrow northern sector, a wider central sector and a narrow southern sector. The study area is located in the central sector where the shelf begins to narrow to the south from its widest point offshore the Thukela River (Fig. 1). The shelf in the study area is narrow (~8 km) (Green et al., 2012a; Cawthra et al., 2012) and steep (2.7°) (Ramsay, 1994) when compared to the global averages of 78 km (Shepard, 1963; Kennett, 1982) and 0.116° respectively (Shepard, 1963). The shelf break occurs at a depth of 100 m (Flemming, 1980) and marks the transition to the steep upper slope (Martin and Flemming, 1988).

This study focuses on the Durban Bight of KwaZulu-Natal. The Durban Bight comprises a crenulated bay bounded to the south by a large headland (The Bluff). There are three main rivers which discharge into the Indian Ocean offshore of Durban. These are (from north to south) the Mdloti, Mhlanga and Mgeni Rivers. The Mgeni River is located nearest to the study area and according to Badenhorst et al (1989); it is the fourth largest river in KwaZulu-Natal to discharge into the Indian Ocean. Goodlad (1986) subdivided the adjoining continental shelf of eastern South Africa into three physiographic zones, which include a very narrow northern sector, a wider central sector and a narrow southern sector. The study area is located in the central sector where the shelf begins to narrow to the south from its widest point offshore the Thukela River (Fig. 1). The study area is narrow (~8 km) (Green et al., 2012a; Cawthra et al., 2012) and steep, with a gradient of 2.7° (Ramsay,1994) compared to the global averages of 78 km (Shepard, 1963; Kennett, 1982) and gradients of 0.116° (Shepard, 1963). The shelf

break occurs at a depth of 100 m (Flemming, 1980) and marks the transition to the steep upper slope (Martin and Flemming, 1988).

2.2. Oceanography and climate

The east coast of southern Africa is considered microtidal, with a predominantly high energy wave-dominated coastline (Smith et al., 2010). Significant wave heights (Hs) of 1.65 m (Corbella and Stretch, 2012) and an average spring and neap tidal range of ~ 1.8 m and ~0.5 m respectively (Moes and Rossouw, 2008) characterise the study area. The recurrence interval of the largest recorded Hs (8.5 m) was estimated to be between 32 and 61 years (Corbella and Stretch, 2012). The maximum wave height (Hmax) within this period was calculated to be 12 m, with a predicted 1:100 year Hmax and Hs of ~13 m and 10 m respectively (Corbella and Stretch, 2012).

The continental shelf of KwaZulu-Natal is characterised by the presence of a strong, poleward flowing western boundary current (the Agulhas Current) that is responsible for the sediment starvation that persists throughout the entire south-eastern margin of Africa (Flemming, 1981; Birch, 1996; Green, 2009a). Where the continental shelf widens, the main flow of the current is located just offshore the shelf break (Schumann, 1987). Inshore of this, a weaker return current (the Natal Gyre) occurs in the inner to mid shelf areas where water is re-circulated northwards (Harris, 1978; Pearce, 1977; de Ruijter, 1999).

The KwaZulu-Natal coastline experiences summer rainfall with dry winters. Durban has an average rainfall of ~1000 mm per year (Jury and Melice, 2000), with average maximum temperatures reaching 32.6 °C and minimum temperatures of 5.8 °C (Mucina et al., 2006) characteristic of a subtropical environment.

Large swells and high energy oceanic storms have been associated with trends in atmospheric circulation (Hirschboeck, 1987). Tyson (1986) identified various weather systems resulting which affect the east coast of South Africa. These include Easterly Waves and Tropical/Subtropical Lows, Westerly Waves and Cut-off Lows, Thunderstorms and Tropical Cyclones/depressions. Guastella and Rossouw (2009)

indicate that cut-off low pressure systems and tropical cyclones are the main progenitors of extreme swells on the KZN coastline. Cold fronts have also been attributed to the production of large swells, but in comparison their influence is less significant (Theron et al., 2010).

2.3. Geological setting

The study area is situated within the Durban basin on the eastern margin on the east coast of South Africa. The Durban basin is a Mesozoic rifted basin; its formation has been attributed to an early phase of extension on the east African continental plate prior to the breakup of Gondwana (Goodlad, 1986; Broad et al., 2006). The preservation of sedimentary sequences on the continental shelf is limited with the majority of sediment transported offshore past the shelf break (Dingle et al., 1983; Green and Garlick, 2011). The main drift sedimentary sequence comprises > 4 000 m of Cretaceous age sedimentary rocks (McMillian, 2003; Green and Garlick, 2011). Along the southern KwaZulu-Natal coast, Early Santonian and Early Campanian age rocks (Cooper and Greyling, 1996) subcrop beneath the latest Quaternary deposits of the Durban harbour (McCarthy, 1967; McMillan, 2003; Green and Garlick, 2011). The latest Quaternary deposits are considered to cover all the Cretaceous units around the Durban area (Green and Garlick, 2011).

Two episodes of crustal uplift and erosion are associated with the deposition of Tertiary aged strata offshore Kwazulu-Natal (Partridge et al., 2006). There are no documented Tertiary exposures or outcrops in the Durban area (Dingle et al., 1983; Roberts et al., 2006), attributed to uplift induced cycles of erosion occurring during the Neogene (Partridge and Maud, 1987). However, Green and Garlick (2011) and Green et al (2013a) considered a series of incised valleys on the shelf to be filled by Pliocene age material and associated with a similar aged shelf-edge wedge. In the deeper portions of the Durban Basin, Cretaceous rocks have been found overlain by Tertiary aged deposits (Dingle et al., 1983; Broad et al., 2006).

Pleistocene and Holocene age sediments occur along the central KwaZulu-Natal coastline as palaeo-dune cordons commonly forming elongate, coast-parallel cemented barrier systems present on the shelf (Martin and Flemming, 1988; Green et al., 2013b; 2014). Unconsolidated transgressive and Holocene age sediments are restricted to a 10-20m thick, inner to middle shelf sediment wedge that comprises the upper-lower shoreface deposits. To date, little is known of the chronology and nature of the shelf deposits that comprise the shoreface. Despite a description of cores from the lower shoreface by Green et al (2012b), no studies have presented a definitive stratigraphy and chronology of the contemporary shoreface. Previous studies on the mid-continental shelf by Green et al (2013b) revealed several closely spaced drowned aeolianite barriers at depths of between 65 m and 50 m. They ascribed these series of prograding ridges with varying orientations to a series of prograded barrier shorelines which segmented a palaeo-lagoonal complex, drowned on the shelf by rapid rise in sea-level during the Holocene deglaciation. The areas that mark the intra-lagoonal depressions of this complex are of prime interest to this dissertation as they are likely to provide preferential accommodation for marine storm-generated deposits within the lower shoreface stratigraphy.

2.4. Sea-level changes

Ramsay and Cooper (2002) provide a synthesis of sea-level variability on the east coast of South Africa (Fig. 2). Following the last glacial maximum (LGM) of ~ 18 000 yrs BP, deglacial sea-level rise has been episodic (Green et al., 2014) with intervals of stillstand superimposed on intervals of rapid sea-level rise. Sea-level stabilised at near present level ~ 6000 yrs BP, after which two minor highstands of +3.5 and +1.5 m at 4500 and 1600 yrs BP occurred (Fig. 3).

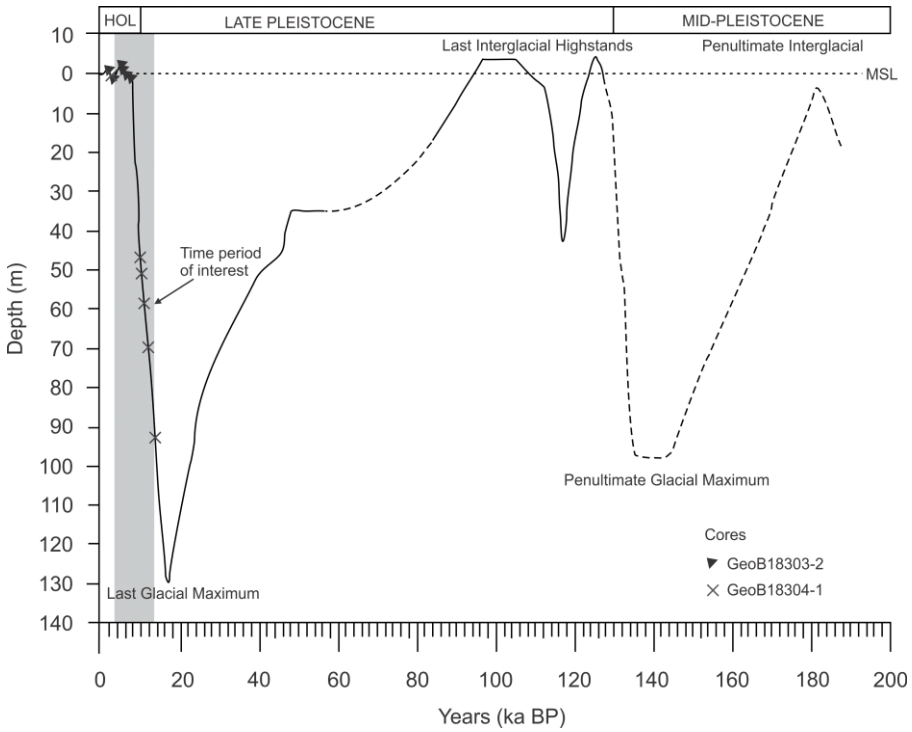

Figure 2. Mid-Pleistocene to Holocene sea level curve for the east coast of South Africa modified after Ramsay and Cooper (2002). Note that the time period of interest spans the period 13 000 yrs BP to the late Holocene. Dates obtained from core material are plotted relative to the sea level curves for both cores GeoB18303-2 and GeoB18304-1.

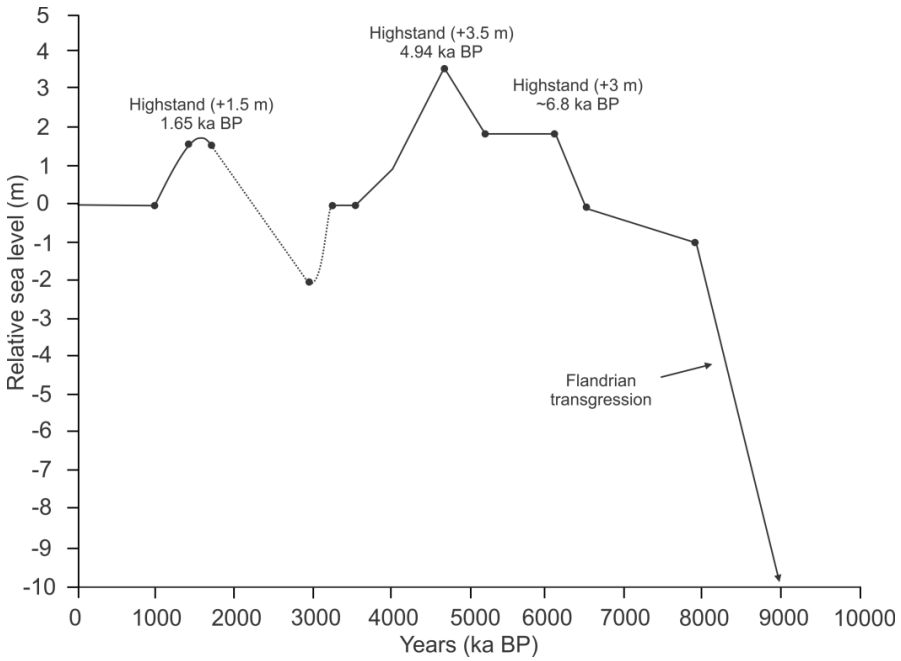

Figure 3. Holocene sea level curve for the East Coast of South Africa modified after Ramsay (1995). Sea-level reached its current position ca. 6.5 ka BP with a maximum highstand of +3.5 m above present sea level followed by subsequent sea-level fluctuations of ~1-2 m.

CHAPTER 3

3.1. Methods and Materials

The majority of the data on which this paper is based were collected during RV Meteor cruise M102 in transit from Le Port, Ile de la Reunion to Walvis Bay, Namibia. The details are discussed below.

3.1.1. Ultra-high resolution seismic profiling

The shallow sub-surface geology was examined using several ultra-high resolution seismic reflection profiles. These were collected using a PARASOUND parametric echosounder aboard the RV Meteor, during cruise M102. Both high and low frequency outputs were collected, however this paper only presents the low frequency output (0.5 kHz) due to signal attenuation of the higher frequency spectra. The data were processed for high and low band pass filtering and gain application and exported as SEGY data for visualisation in the Kingdom Suite software package. The processed data resolve to ~ 10 cm in the vertical domain with a maximum penetration of ~ 20 m in localised areas. In all lines, the upper 5 m of the seafloor sediment package were resolved with a high level of detail.

3.1.2. Coring

Key targets were identified from the ultra-high resolution seismic packages for further analysis by coring. Several coring techniques were attempted on the Durban shelf. Gravity coring was the least successful, with limited penetration (< 10 cm) due to a hard upper sandy package against which the core barrels were refused. Vibrocoring was more successful, with three vibrocores being acquired, two of which (GeoB18303-2 and GeoB18304-1) are described in this study. The corer comprised a standard marine vibrocorer capable of acquiring cores of up to 5 m in length and 10 cm in diameter. Cores were split onboard and logged according to standard sedimentological procedures. Sub-sampling at 5cm intervals for grain size analyses was undertaken,

together with sampling for material suitable for AMS C^{14} dating. A total of 13 samples were collected from cores GeoB18303 and GeoB18304 for dating purposes. The material used for AMS C^{14} dating is discussed in Table 1. All shell material was selected from in-situ life position, especially in the case of bivalves that were still articulated. Wherever possible, the most intact shells were chosen with the least amount of bleaching of the shell exterior.

3.1.3. Multibeam bathymetry

Multibeam bathymetry collected by the eThekweni Municipality and described in Green et al (2012a, 2013b) was integrated with the ultra-high resolution seismic and core data in order to assess the spatial distribution of tempestite signatures on the lower Durban shoreface. In particular, the modern signatures of tempestites were assessed (cf. McMullen et al., 2015). A 20 km^2 portion of seafloor was mapped using a Furuno 160-KHz WMB-160F multibeam echosounding system (Furuno, Nishinomiya, Japan). Positions and attitude estimations were provided by a Furuno SC30 system. All data were corrected to depth relative to Mean Sea Level (MSL) after reconciliation with sound-velocity profiles and tidal fluctuations. The data resolve to ~5 m in the horizontal domain and ~ 10 cm in the vertical domain.

3.1.4. Grain size analysis

Particle size analysis was undertaken for both the bulk and terrigenous sediment fractions at a down-core sample resolution of 5 cm. The samples were sieved to obtain the bulk grain size distribution with the result of the analysis presented as phi values where the mean, median, sorting and skewness were calculated using the Folk and Ward equations. $CaCO_3$ was analysed at the identical resolution as the grain size data using a gaseometric carbonate bomb technique.

In addition, 1-2 g of the bulk sediment sample were analysed for the grain-size distribution of the terrigenous fraction where the sediment samples were treated with

10% HCl, H_2O_2 and NaOH to remove calcium carbonate, organic matter, and biogenic opal, respectively. The samples were then suspended in demineralised water with the addition of $Na_4P_2O_7$ to prevent the formation of aggregates. The particle size distribution was measured with a Coulter laser particle sizer LS 13 320 (MARUM, University of Bremen, Germany) generating 92 size classes from 0.4 to 2000 μm. For this study the mean grain-size data are displayed as phi (Appendix II; Tables 7 and 8).

3.1.5. Geochemical and mineralogical analyses

Sampling at a resolution of 5 cm was undertaken for further geochemical and mineralogical analyses. Additional samples were collected at selected locations corresponding to significant results obtained from the grain size and $CaCO_3$ content analyses. Sample pre-treatment consisted of drying and grinding for 120 seconds in a silicon nitride vessel to prevent contamination (Planetary Micro Mill PULVERISETTE 7 premium line, MARUM, University of Bremen, Germany), to assure that all particles were smaller than 63 um.

3.1.5.1. Bulk geochemistry (XRD)

Selected horizons were sampled for X-ray diffraction (XRD) mineral identification in cores GeoB 18303-2 and GeoB 18304-1. To test the working hypotheses X-ray diffraction pattern analyses have been done in the laboratories of the research group Crystallography (University of Bremen, Central Laboratory for Crystallography and Applied Material Sciences, ZEKAM, Dept. of Geosciences). Dried Bulk samples were dried and ground (<20 μm particle size) and prepared with the Philips X'Pert Pro multipurpose diffractometer equipped with a Cu-tube (kα 1.541, 45 kV, 40 mA), a fixed divergence slit of ¼°, a 16 sample changer, a secondary Ni filter and the X'Celerator detector system. The measurements were done as a continuous scan from 3 – 85° 2θ, with a calculated step size of 0.016° 2θ (~ 50s/step). Mineral identification was done using Philips X'Pert HighScore™ software and Apple MacIntosh MacDiff 4.25.

Quantification of the bulk fractions mineral assemblages of was via the QUAX full pattern method (c.f. Vogt et al., 2002).

3.1.5.2. Elemental Analysis (XRF)

Elemental compositions were measured on 205 sediment samples collected at a resolution of 5 cm. Pressed pellets composed of 4 grams of each sample compressed at 25 kPa, were used to analyse for major, minor and trace element composition (Panalytical epsilon 3 XL, Bremen University, Germany). USGS and Chinese rock and sediment standard reference material GBW 07316 was prepared simultaneously and used to calibrate all measured results. Analyses of the reference material gave results within +- 10% of certified values (Appendix I; Tables 3 and 4).

3.1.6. Storm wave modelling and sediment mobility threshold

Analyses of the Durban wave records indicate that the March 2007 storm was the highest magnitude event recorded offshore KZN (Corbella and Stretch, 2012; Salzmann and Green, 2012). This event was characterized by significant wave height of 8.5 meters, peak wave period of 16.6 seconds and a SSE to SE (147^0) storm swell approach direction (Salzmann and Green, 2012). The wave form for this event was modelled using SWAN (Booij et al., 1999, Ris et al., 1999) which was initialised at the offshore boundaries with parametric inputs from the March 2007 event.

SWAN is a depth and phase-averaged, third-generation wave model that simulates the refractive propagation and evolution of the wave spectrum. It was implemented on a HPC (High-Performance Computing) cluster with 40 processors, and run in stationary mode, i.e. time is removed from the computations and waves are assumed to propagate instantaneously across the modelling domain. A regular structured grid with 5 meters resolution was used for representing the computational domain. SWAN was run in third generation mode, using default parameters in order to account for bottom friction

dissipation, non-linear wave interaction, diffraction and white capping dissipation (c.f. Loureiro et al., 2012; 2013).

Considering the dependency of near-bed sediment movement on the bottom orbital velocity amplitude (Soulsby, 1997), outputs from SWAN included the root mean square values of the near bottom orbital velocity (Urms) for the entire modelling domain, computed considering a JONSWAP empirical bottom friction model and linear wave theory (Holthuijsen, 2007).

To evaluate the potential for wave-induced coarse sediment mobility during modelled storm conditions, the threshold bottom orbital velocities (Uwcr) were computed for several grain size classes according to empirical approximation of Komar and Miller (1974):

Uwcr = [1.09g(s-1)]4/7d3/7T3/7 for d > 0.5 mm

Where, g is acceleration due to gravity; s is the ratio of densities of grain and water; d is the mean sediment diameter and T the wave period.

CHAPTER 4

4.1. Results

4.1.1. Seismic stratigraphy

The entire area is underlain by an acoustic basement comprising Cretaceous age siltstones (Green and Garlick, 2011). These are intersected by notable subaerial unconformities that take the form of several wide (~400 m) and deeply (100 m) incised valley forms (Green et al., 2013a). Overlying these are several packages of both consolidated and unconsolidated material (Fig. 4). The consolidated material comprises pinnacles of aeolianite and beachrock (Green et al., 2013b; Pretorius et al., 2016). The unconsolidated material remains the focus of this study.

The overlying unconsolidated material can be divided into two distinct packages (Unit A and B) (Table 1). Unit A comprises a moderate amplitude, onlapping sub-parallel reflector package. It onlaps the valleys walls within the subaerial unconformity (u/c), and comprises the lower fill unit of these features (Fig. 4a and c). This is truncated by a moderate amplitude reflector, seen only in the fill succession (Surface i). Surface i is notable for its small (> 1m deep) incisions. Sub-unit A1 occurs as isolated lenses of seaward prograding, low amplitude parallel reflectors. This is erosionally truncated by a high amplitude reflector (Surface 1). This surface is regionally occurring and caps the aeolianites/beachrock ridges, truncates the incised valley fills and underlies Unit B.

Unit B comprises six discrete Sub-units. Sub-unit B1 occurs in the deeper, seaward portions of the shelf. It is composed of parallel reflectors that onlap the subaerial unconformity in an aggradational manner a series of chaotic to parallel reflectors. It is located at depths of more than 68 m, where the subaerial unconformity begins to dip more steeply seawards (Fig. 4). Sub-unit B2 occurs as a series of seaward prograding, oblique-parallel, moderate amplitude reflectors. In some places, the internal configuration is unclear and the Sub-unit is acoustically opaque (Fig. 4a). Sub-unit B3 consists of irregular, wavy to chaotic high amplitude reflectors. This occurs in isolated instances (eg. Fig. 4a). Unit B4 comprises irregular, seaward dipping, sigmoid prograding reflectors that are toplapped by Surface ii. This surface is irregular, with

undulating relief. This relief is infilled with Sub-unit B5, another series of irregular, wavy to chaotic high amplitude reflectors (Fig. 4b and 4c). These onlap high points in Surface 1, especially where Surface 1 is expressed as saddles between aeolianites/beachrock ridges. This Sub-unit occurs at depths of ~ 60 to 16 m and is best expressed where there are the fewest topographic disturbances by aeolianites/beachrock ridges along profile.

Table 1. Seismic stratigraphic observations and interpretations off the Durban continental shelf in central KwaZulu-Natal. Seismic units are defined as Unit A and Unit B which are further subdivided based on internal configurations. Descriptions of these units are provided which include the underlying surface, seismic characteristics, spatial distribution and cross sectional thickness of individual units. Based on these observations the environment of deposition is then inferred.

Unit		Underlying surface	Modern description	Stratal relationship	Thickness	Interpreted depositional Environment
B	5	Surface ii	Shore attached wedge	Irregular, wavy to chaotic high amplitude reflectors	8 m	Contemporary shoreface
	4	Surface 1	Proximally located aggrading/prograding sigmoidal sediment wedge	Irregular, seaward dipping discontinuous reflectors toplapped by surface ii	8 m	Tempestite
	3	Surface 1	Landward thinning wedge onlapping surface 1 and aeolianites/ beachrock ridges	Irregular, wavy to chaotic high amplitude reflectors	4 m	Tempestite
	2	Surface 1	Discontinuous outcrops	Prograding, oblique parallel moderate amplitude reflectors which onlap Surface 1	4 m	Middle to lower shoreface
	1	Surface 1	Occurs at depths of 68 m and more in the deeper, seaward portions of the shelf	Parallel reflectors that onlap the underlying surface in an aggradational manner, a series of chaotic to parallel reflectors	6 m	Middle shoreface
A	Ai	Surface i	Upper incised valley fill	Seaward prograding, low amplitude parallel reflectors	5 m	Flood tide delta
	A	u/c	Lowermost incised valley fill	Moderate amplitude high angle, chaotic to draped parallel reflectors which onlap the valley wall	11 m	Central Basin

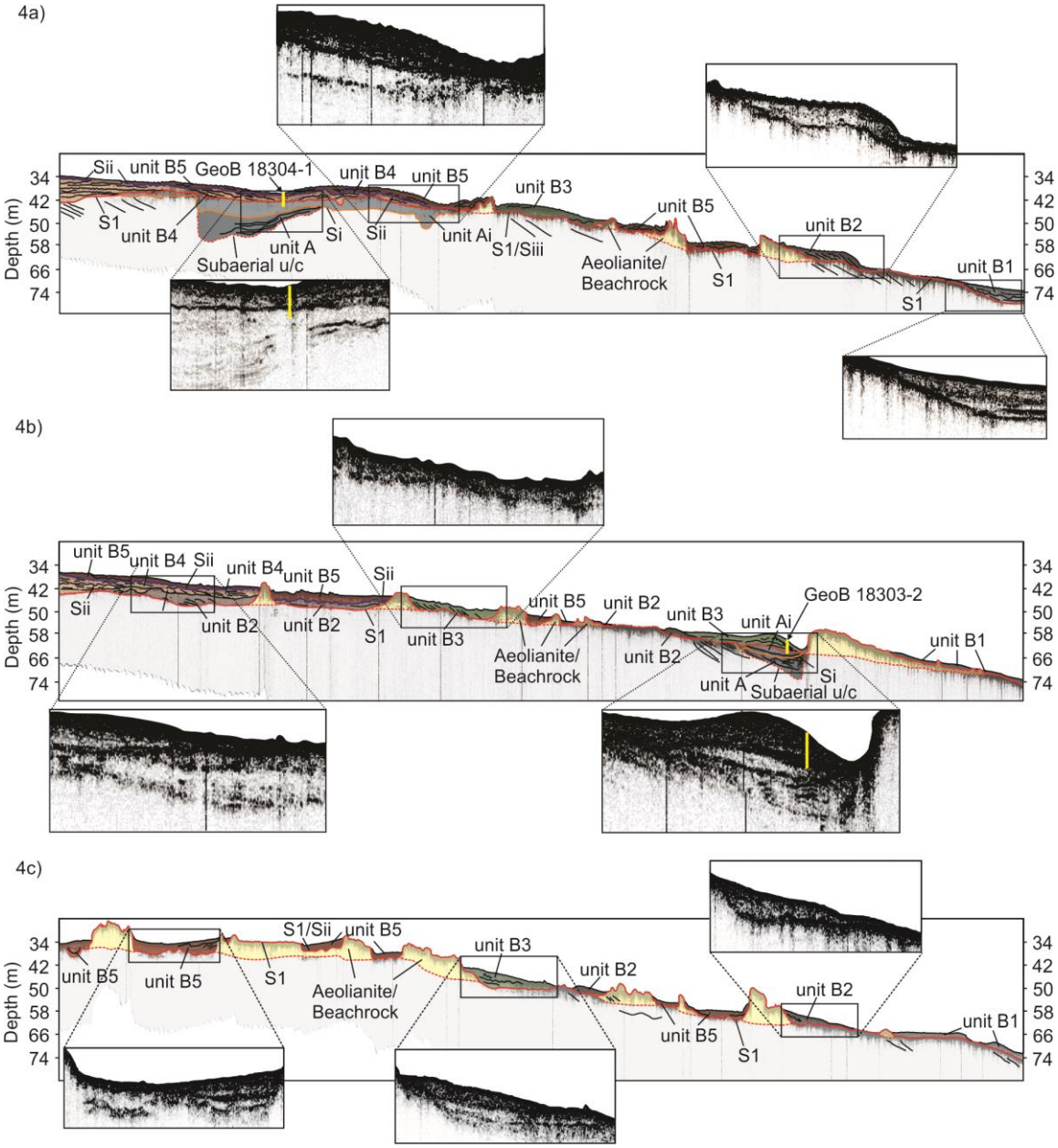

Figure 4. Shore-perpendicular seismic profiles (locations are depicted in figure 1). Aeolianite/beachrock ridges are shown as yellow. Note the covering of Unit B in all sections. a) Unit A infills the topography formed in the subaerial u/c. Unit B1 is restricted to the transition to the outer shelf. Unit B2 and unit B3 onlap the seaward edge of the aeolianites/beachrock ridges. b). Unit B3 occurs as isolated reflector packages with a more chaotic internal reflector configuration than Unit B2. Unit B4 is restricted to depths of 30-40 m and occurs as isolated packages truncated by surface. c) Unit B5 marks the uppermost layers in the inner shelf regions.

4.1.2. Core lithology

The cores obtained were composed of sediment ranging from very fine sand to cobbles in size (Fig. 5). The material present was dominated by disaggregated shell debris, with isolated organic rich material. These form a range of facies based on the relative abundances of the sediment types, textures, structures and relative thicknesses. The proximal and distal core were obtained from various water depths corresponding to -38.2 m and -68 m amsl, respectively.

4.1.2.1. Facies successions

The basal horizon of the most seaward core (GeoB18304-1) contains a 9 cm thick layer, composed of very fine muddy sand with occasional shell debris (facies 1) and constitutes the finest equivalent of the core material (Fig. 5). Facies 2 consists of medium sand exhibiting fining upward sequences with minor silt and shell debris, occasionally containing whole shells and grit. Coarse sand bearing shell debris and grit sized sediment (facies 3) is commonly associated with finer sediment of facies 2. Facies 4 represent horizons containing the coarsest sediment fraction (very coarse sand), with high percentages of grit and shell debris. Horizons composed of shell hash range from very coarse sand to pebble in size (facies 5), occasionally containing whole shells and displaying coarsening upward trends. However fining upward sequences are also present but are commonly expressed by the finer sediment packages. Core GeoB18303-2 contains clasts of calcareous cemented material, together with mudballs at various elevations. The calcareous cemented material is similar in composition to the encasing material; the fragment's presences are associated with facies 4 and facies 5, with the size of the framework clasts of the lithic fragment similar to that of the surrounding material. They occur at core depths of 1.90 m, 3.00 m and 4.55 m (Fig. 5). The presence of mud balls are associated with a single substantially thick unit of facies 4 at a core depth spanning 1.90 m to 3.05 m. Core GeoB18304-1 displays regularly interspersed horizons of medium sand (facies 2), interbedded with coarser material (facies 3 and 5, Fig. 5).

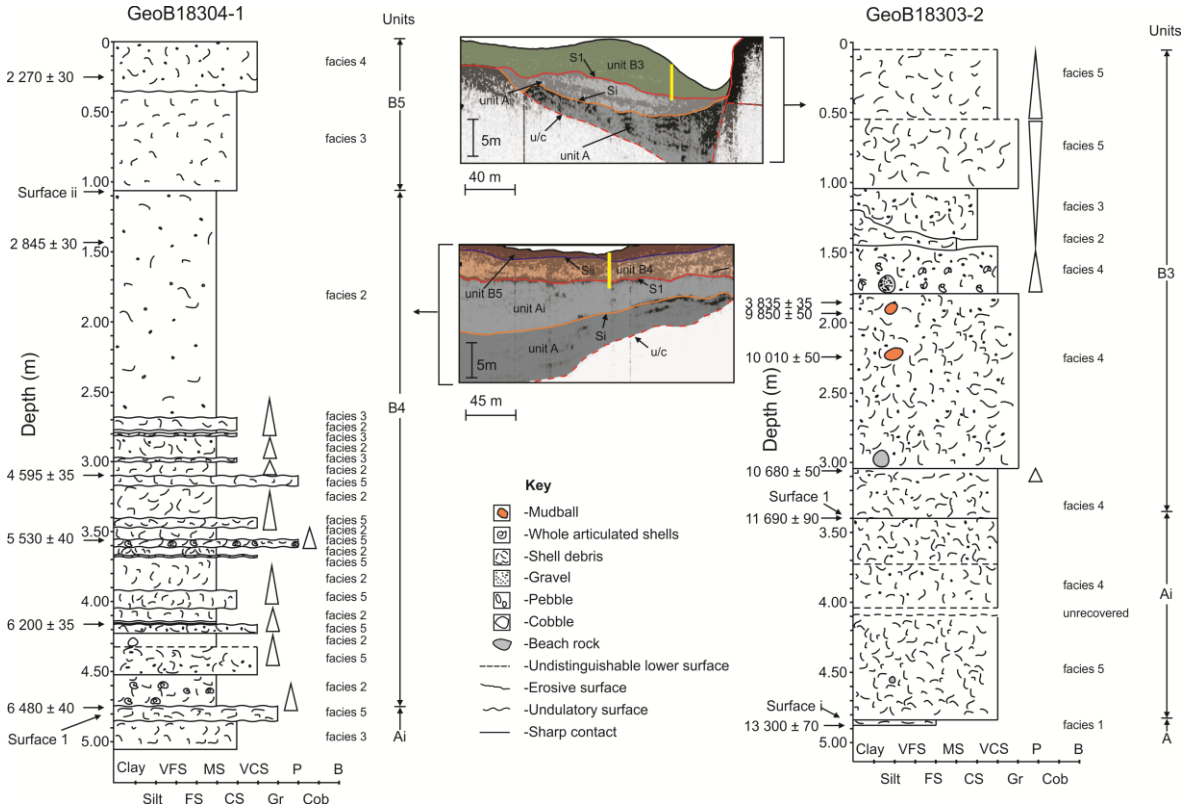

Figure 5. Graphic logs of cores GeoB18304-1 and GeoB18303-2 with associated sedimentary facies. Note the location of the core relative to the seismic units B5, B4 and unit Ai in core GeoB18304-1 and unit B3 and units Ai and A in core GeoB18303-2. The lower margin of unit B4 consists of alternating shell hash horizons interbedded with finer sediment. Facies 3 contains organic rich mudballs encased in coarse shelly sediment. Dates obtained and surfaces intersected are indicated along the depth profile of the sedimentary logs.

4.1.2.2. Grain size

The removal of calcium carbonate, organic matter, and biogenic opal had a significant effect on the overall grain size distribution when compared to the bulk grain size of the sediment (Fig. 6a and Fig. 7a). The terrigenous sediment is significantly finer, and in most cases displays similar trends with the bulk grain size data. Several departures between the two are however evident (Appendix II, Tables 7 and 8).

The uppermost portion of the most proximal core (GeoB18304-1) is composed of coarse sand (Fig. 5), with a sharp decrease in grain size at approximately 0.35 m depth (Fig. 7a). At depths between 0.35 to 3.10 m the grain size remains constant with minor

fluctuations (Fig. 7a). There is a clear departure in trend from the bulk and terrigenous sediment grain sizes at 2.5 m down-core, where the terrigenous sediment shows a sharp peak in fine sediment. This deviation does not correlate with the bulk grain size results (which displays a consistently similar grain size at these depths down core). Upon comparison with the XRF results it was evident that there were no correlations with elemental concentrations and therefore this deviation in the terrigenous sediment grainsize may be a result of low obscuration levels during sample analyses. Below 3.10 m depth an overall increase in the bulk grain size is evident with distinct variations in grainsize. These are associated with the occurrences of the shell hash of facies 5. In contrast, the trends displayed by the terrigenous sediment show a significant decrease in overall grainsize below 3.10 m depth where clearly shelly material dominates. Several very fine layers are evident, corresponding to fine sands (Fig. 5). This is particularly notable at core depths of 3.70 – 3.85 m, 4.35 m and 4.60-4.80 m (Fig. 7a). On the whole, the finest material is always derived from the terrestrial fractions.

Despite being the most distal core, the grain size of GeoB18303-2 is significantly coarser than GeoB18304-1 (Fig. 6a and Fig. 7a). Overall, the bulk sediment analyses reveal a consistent grain size with depth in contrast with terrigenous sediment which increases in grain size with depth (Fig. 6a). Two peaks are present which display a significant increase in finer sediment associated with the presence of organic rich clasts composed of fine grained material. These peaks are located at -1.95 and -2.25 m depth and can be seen in both the bulk and terrigenous sediment grain sizes (Fig. 7a). Remarkably coarser peaks in the bulk sediment grain size occur at 3.15 m and 4.55 m. It is notable that the package of sediment from 1.80-3.05 m is almost entirely comprised of very coarse sand (refer to Fig. 5).

4.1.3. Elemental chemistry

The down core profile of the elemental concentrations reveals distinct trends in both cores (Fig. 6b and Fig. 7b). This paper examines correlations between elements that group into two main geochemical groups: the terrigenous fraction (Al, Si, K, Ti and Rb) and marine fraction (Ca and Sr) (Gebhardt et al. 2008; van Rooij et al. 2007; Vidal et

al., 2002; Grützner et al., 2003; Arz et al., 2001 and 2003; Kuhlmann et al., 2004b; Romero et al. 2008; Calvert and Pederson 2007). Other elements which show partial affinities to the terrigenous fraction are Fe, Zr and S with clear variability in the lower sections of the most distally located core (GeoB18303-2) that tend to match the terrigenous fraction trends (Fig. 6b). It should be noted that the concentration of S in the most proximally located core (GeoB18304-1) shows an inverse relationship with these elements (Fig. 7b) (Appendix II; Tables 3 and 4).

4.1.3.1. Down-core distribution

The results of the XRF analyses of the distal core GeoB18303-2 indicate that Ca and Si are the major elements present with respective concentrations of 24.617 and 10.189 wt %, followed by minor concentrations of Al (1.154 wt %), K (0.57 wt %), Fe (0.562 wt %), S (0.245 wt %), Sr (0.163 wt %), Ti (0.142 wt %) and trace concentrations of Zr (0.028 wt %) and Rb (0.003 wt %).

At depths of 1.45, 1.95 and 2.25 m distinct changes in elemental concentrations are evident (Fig. 6b). At 1.45 m, the abundance of Ti, Zr and Si increase abruptly (0.338, 0.058 and 19.221 wt %, respectively) and are matched by a converse decrease in the abundance of Ca and Sr (14.660 and 0.099 wt %). This change is not reflected in the general trend of Rb which appears to be mostly constant (Fig. 6b). The sharp change in abundances is correlated to an erosional surface identified in the core (Fig. 5).

The most significant changes in concentration occur at depths of 1.95 m and 2.25 m respectively. Here significant decreases in the concentration of the marine fraction elements including Ca (10.376 wt %) and Sr (0.174 wt %) are evident (Fig. 6b). Associated with these depths are protracted increases in the terrigenous fraction elements including Si (20.491 wt %), Al (4.157 wt %), K (1.597 wt %), Ti (0.319 wt %) and Rb (0.007 wt %), as well as an increase in Fe (2.015 wt %) and S (0.809 wt %).

The concentration of elements including as Al, K, S and Rb display consistent concentrations and little variability with depth down core; Si, Fe, Ti and Zr are however present in higher concentrations to a depth of 1.45 m (Fig. 6b). Below this depth the

abundances of terrigenous elements decrease, with an associated increase of carbonate fraction elements. The lowermost unit sampled, unit Ai revealed increased levels of Si (22.138 wt %), Al (2.731 wt %) and Fe (1.058 wt %).

The XRF analyses of the proximal core GeoB18304-1 indicate that Ca and Si are the major elements present with concentrations of 18.004 and 16.577 wt % respectively, followed by minor concentrations of Al (1.183 wt %), Fe (0.661 wt %), K (0.432 wt %), Ti (0.161 wt %), S (0.158 wt %), Sr (0.117 wt %), and trace concentrations of Zr (0.025 wt %) and Rb (0.002 wt %).

Elemental concentrations in depth down core tend to be very subtle, typically displaying very little variation to a depth of 3.15 m (Fig. 7b). From this depth down to the basal layers, there is an increase of marine fraction elements which include Ca (27.379 wt %) and Sr (0.193 wt %) with an associated peak in concentration of S (0.236 wt %). At this depth there was a decrease in elemental concentrations of Si (8.160 wt %), Al (0.681 wt %), Fe (0.465 wt %), Ti (0.108 wt %) and Zr (0.025 wt %). The concentration of K and Rb is very homogenous with depth displaying very little correlation with subsequent elemental abundances. Below 3.15 m depth the elemental abundances display significant variation down core with Ca, S, and Sr following the same trend with significant peaks at 4, 4.15, 4.45 and 4.8 m depths. At these depths there is also a significant decrease of Si, Al, Fe, Ti and Zr. It is worth noting the multiple spikes in increased abundances of the marine elements, occurring rhythmically towards the core base (Fig. 7c).

4.1.3.2. Correlation with grain size and XRF

When comparing the elemental concentrations of the proximal and distal cores, it is evident that core GeoB18303-2 has a higher concentration of carbonate fraction elements (Ca and Sr) and a coarser grainsize of both the bulk and terrigenous sediment (Fig. 6a and 6b). An increase in the concentration of the terrigenous fraction elements at depths of 1.45, 1.95 and 2.25 m is also associated with a finer grainsize. In core GeoB18304-1 the grain size is fairly consistent with minor fluctuations to a depth of

3.15 m, below this depth cyclic fluctuation in grainsize is apparent with coarser material associated with the rhythmic peaks in abundances of Ca and Sr (Fig. 7a and 7b).

4.1.3.3. XRD

The elemental abundances in both cores show similar crude down-core trends as to the trace element geochemistry (Fig. 6 and Fig. 7). Core GeoB18303-2 is dominated by $CaCO_3$ (34 wt% average), with lesser amounts of Quartz (31 wt%). The inverse relationship between Quartz and $CaCO_3$ is strongly evident in core GeoB18303-2 with the strongest correlation present at a depth of 2.1 m corresponding to facies 4 of unit B3. Spikes in $CaCO_3$ occur at 1.6 m and 2.1 m depth. Peaks in Quartz and K-Feldspar are associated with horizons dominated by mudballs at depths of 1.95 m and 2.15 m (Fig. 6c) (Appendix I; Table 5 and Table 6).

In core GeoB18304-1, Quartz is the dominant mineral (by wt%), comprising up to 47% in some samples. There is a similar inverse relationship between the Quartz and $CaCO_3$ weight percentages, the lowest measured value of Quartz was 30.284 wt % in contrast to the highest measured $CaCO_3$ value of 49.895 wt % at a depth of 3.15 m. Low weight percentages of Quartz are always associated with smaller lower bulk grain sizes and with increased concentrations of the terrestrial elements Si, Al, Fe, Ti and Zr (Fig. 7a, b and c). Sharp decreases in the weight percentage of K feldspar (2.159 wt %) and Plagioclase (4.065 wt %) are common (Fig. 7c) and are associated with the peaks in $CaCO_3$. These occur at depths of 3.15 m and 3.45 m respectively.

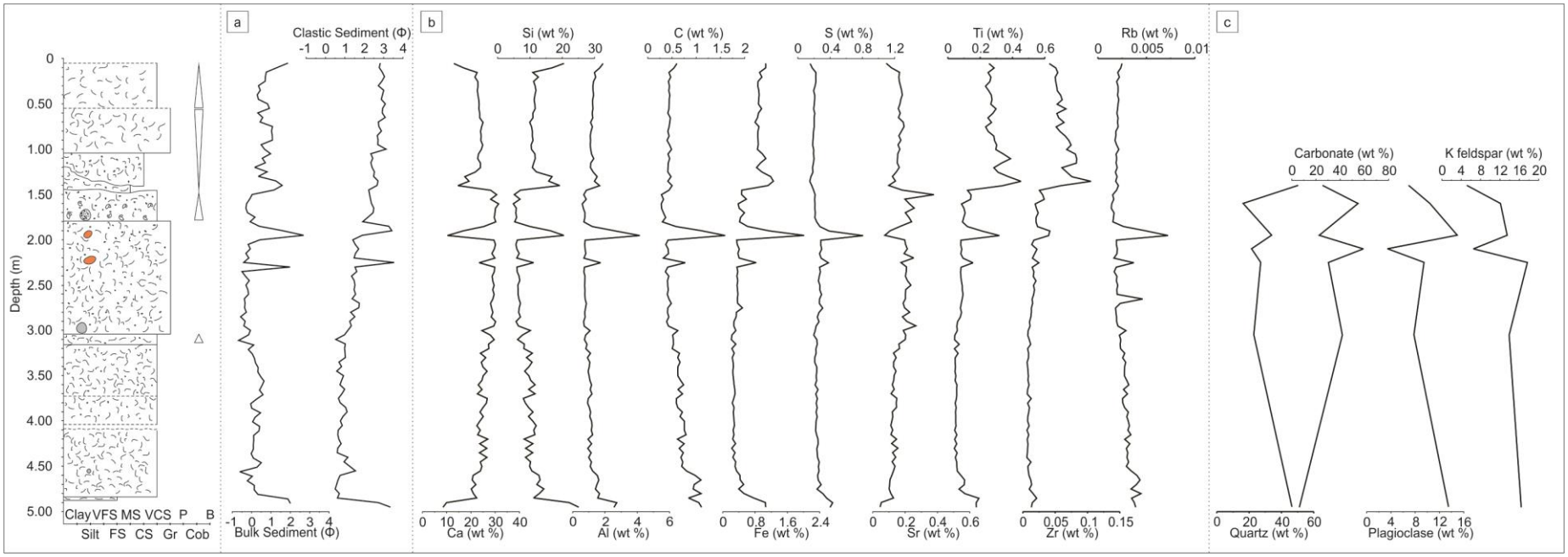

Figure 6. Sedimentology, grain size, elemental chemistry and mineralogy of core GeoB18303-2. All depths are relative to the collar of the core. a) Grain size data for both the bulk and terrigenous sediment fractions measured in phi (Ø). b) Down-core XRF elemental chemistry. Note the strong correlations of elements below 1.45 m depth. Also note the strong terrigenous elemental signatures from depths characterised by mud balls. c) XRD Mineral concentrations.

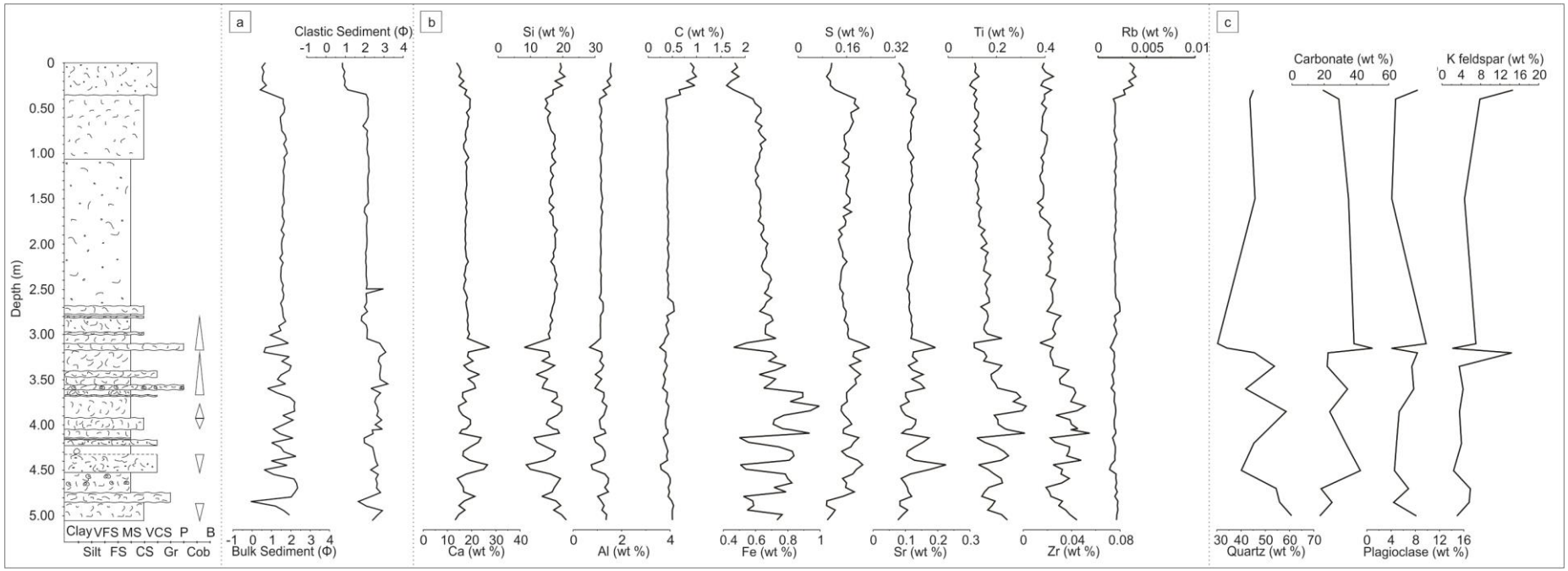

Figure 7. Sedimentology, grain size, elemental chemistry and mineralogy of core GeoB18304-1. All depths are relative to the collar of the core. a) Grain size data for both the bulk and terrigenous sediment fractions measured in phi (Ø). Note the inverse relationship between the bulk and terrigenous sediment is present below depths of 3.15 m. b) Down-core XRF elemental chemistry. Note the strong correlation of elements at depths below 3.15 m. c) XRD Mineral concentrations.

4.1.4. Chronostratigraphy

The oldest material cored was that of seismic Unit A1 which was intersected by cores GeoB18303-2 and GeoB18304-1 (Table 2). The uppermost portion of Unit A1 was intersected by both cores, and material within facies 1 from the most distal core whereby the total organic carbon (TOC) content was dated at 13 300 ± 70 cal yr BP. Surface 1 marks the uppermost limit of Unit A1, in the proximal core this surface was marked by the presence of articulated bivalves belonging to the species Eumarcia paupercula which was dated at 6 480 ± 40 cal yr BP (facies 5) and distally at 11 690 ± 90 cal yr BP through subsampling the organic rich sediment and dating the TOC of the lower flood tide deltaic sediment.

In GeoB18303-2, Surface 1 is overlain by coarse material of Unit B3 which dates from 10 680 ± 50 cal yr BP (subsampled carbonate rich material corresponding to the reworked lower shoreface) to 3 835 ± 35 cal yrs BP. A mudball at 2.25 m was dated at 10 010 ± 50 cal yr BP. Another mudball located at a depth of 1.9 m revealed several ages. The surface coating of stiff mud was dated at 3 835 ± 35 cal yr BP and the core material yielded a date of 9 850 ± 60 cal yr BP.

The material directly above Surface 1 in the most proximal Core GeoB18304-1 dates from between 6 480 ± 40 cal yr BP to 2 270 ± 30 cal yr BP (bivalve hosted in facies 5). Unit B4 is composed of medium sand to coarse shelly sediment of facies 2 and 3 respectively and spans from 6 480 ± 40 cal yr BP (facies 5) to sometime after 4 595 ± 35 cal yr BP (dated whole shell). This material is directly overlain by Unit B5 which yielded a date of 2 845 ± 30 cal yr BP (gastropod, Nassarius sp.) to present day.

Table 2. Chronostratigraphy of GeoB18304-1 and GeoB18303-2. AMS radiocarbon dates are indicated, together with the composition of material dated, interpretation of the intersected unit/bracketing surface and the associated sedimentary facies.

Depth down core	Calibrated AMS Radiocarbon age (yr BP)	Material Dated	Remark	Interpretation (Unit/Surface)	Facies
Core GeoB18304-1					
0.25 m	2 270 ± 30	Bivalve	$CaCO_3$	Contemporary shoreface, unit B5	facies 4
1.45 m	2 845 ± 30	Single gastropod, Nassarius sp	$CaCO_3$	Storm-generated gravel/sand couplets, lower shoreface, unit B4	facies 2
3.1 m	4 595 ± 35	Whole shell	$CaCO_3$	Storm-generated gravel/sand couplets, lower shoreface, unit B4	facies 5
3.59 m	5 530 ± 40	Articulated bivalve, life position, Eumarcia paupercula	$CaCO_3$	Just beneath capping horizon between incised valley fill (Unit Ai) and ebb tide storm deposit, the wave ravinement surface	facies 5
4.18 m	6 200 ± 35	Articulated bivalve, life position, Eumarcia paupercula	$CaCO_3$	Upper incised valley fill, likely to represent flood tide deltaic sand body, Upper unit Ai	facies 5
4.76 m	6 480 ± 40	Articulated bivalve, life position, Eumarcia paupercula	$CaCO_3$	Upper incised valley fill, likely to represent flood tide deltaic sand body, unit Ai	facies 5
Core GeoB18303-2					
1.9 m	3 835 ± 35	Bulk organic carbon (outer rim)	Total Organic Carbon	Mudball, lower shoreface deposit. unit B3	facies 5
1.9 m	9 850 ± 50	Bulk organic carbon (centre)	Total Organic Carbon	Mudball, lower shoreface deposit. unit B3	facies 5
2.25 m	10 010 ± 50	Bulk organic carbon	Total Organic Carbon	Mudball, lower shoreface deposit. unit B3	facies 5
3.03 m	10 680 ± 50	$CaCO_3$ sediment	$CaCO_3$	Reworked lower shoreface material, overlying surface 1, unit B3	facies 5
3.4 m	11 690 ± 90	Bulk organic carbon	Total Organic Carbon	Incised valley fill, flood tide deltaic package, underlying surface 1 (wave ravinement surface), unit Ai	facies 4
4.89 m	13 300 ± 70	Bulk organic carbon	Total Organic Carbon	Incised valley fill, flood tide deltaic package, unit Ai	facies 1

4.1.5. Bathymetry and wave modelling

The bathymetry reveals two distinct types of seafloor. Rugged seafloor, with outcroppings of the beachrocks/aeolianites dominates the study area (Fig. 8). Areas of smooth/low relief seafloor coincide with the zones of unconsolidated material identified as seismic unit B and reconciled with the material recognised in the cores. These areas of seafloor lack perturbations, are generally smooth and have undisturbed gently seaward-dipping profiles. Occasional irregular mounds are apparent between depths of 40 to 60 m. These range in relief from 50 to 100 m. The most significant sediment mound is associated with the prominent beachrock/aeolianite ridge at 60 m depth (cross sections b-b' and d-d', Fig. 8). At depths below 40 m the gradient of the continental shelf shallows and the mounds are no longer apparent.

SWAN model results that incorporate both bathymetry and theoretical sediment movement in the context of the contemporary wave climate are displayed in figure 9. The gravel fraction (> 2 mm) was chosen as most significant as this comprises the coarsest fractions of the core material. The threshold Urms value of 0.52 m/s was obtained for gravelly sediments (d= 2mm). Figure 9b represents the Urms values for the entire modelling domain, with areas below the Urms threshold value for gravel blanked. In the remaining areas there is an increase in potential sediment mobility as water depths decrease and bottom orbital velocities increase. This is particularly noticeable in the shallow south western extreme of the modelling domain, an area of enhanced wave and sea bottom interaction, where orbital velocities are consistently above 1 m/s given water depths of approximately 20 meters.

It is clear that the threshold wave orbital velocities (Urms) required to move gravel in relation to the largest recorded storm wave (Hs = 8.5 m) are not achieved in areas where the bathymetry is smooth, especially where the cores were collected (Fig. 9b). Furthermore, there appears to be no preferential area where gravel could be deposited at depths associated with the core sites.

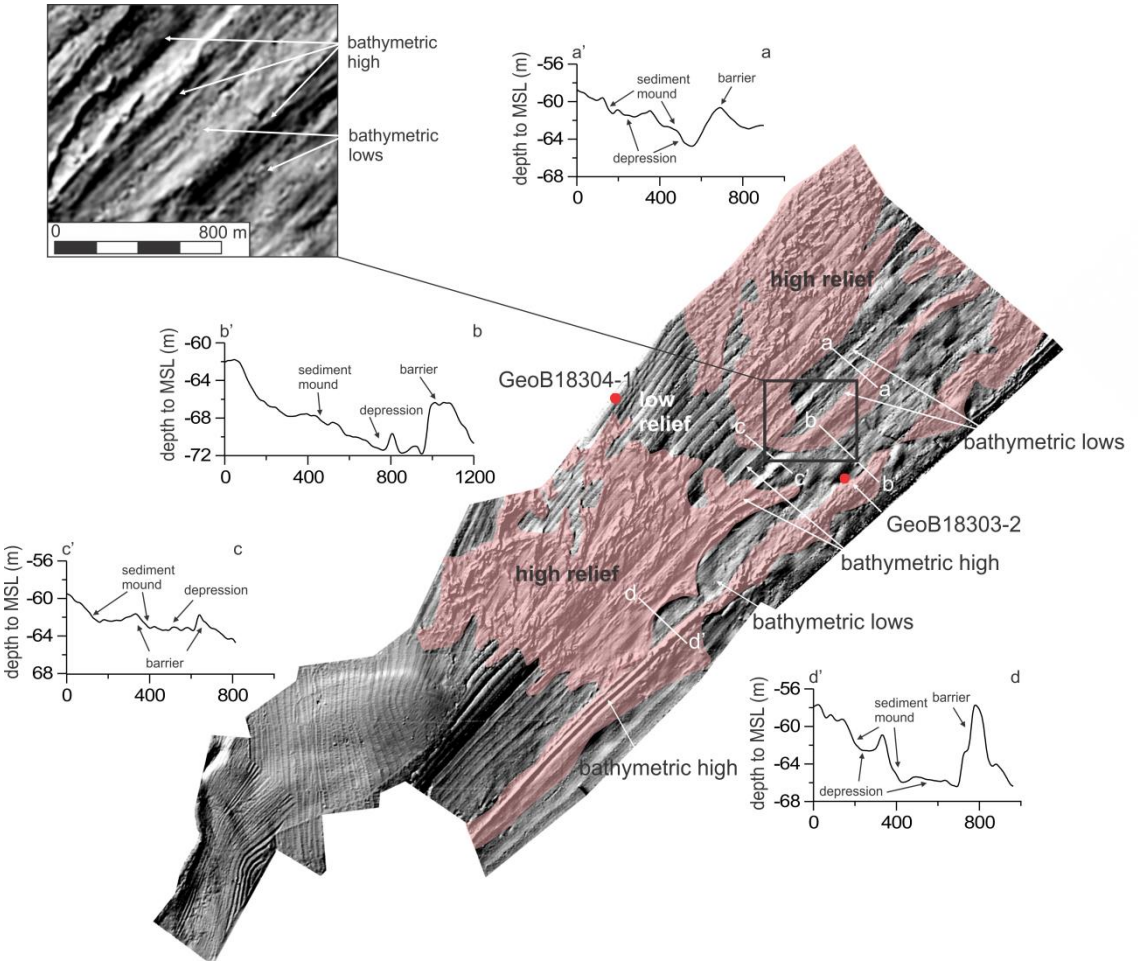

Figure 8. Multibeam bathymetry of the study area. Note the two discreet seafloor types marked by rugged seafloor relief and smooth featureless seafloor relief. The high relief areas represent outcrop of beachrock/aeolianites, whereas the low relief areas are marked by unconsolidated sediment. Isolated mounds of unconsolidated sediment occur sporadically at depths of between 40 m and 60 m. Upper left image displays a portion of the seafloor bathymetry in further detail, the bathymetric lows are of particular interest as they are associated with sediment accumulation on the sea floor.

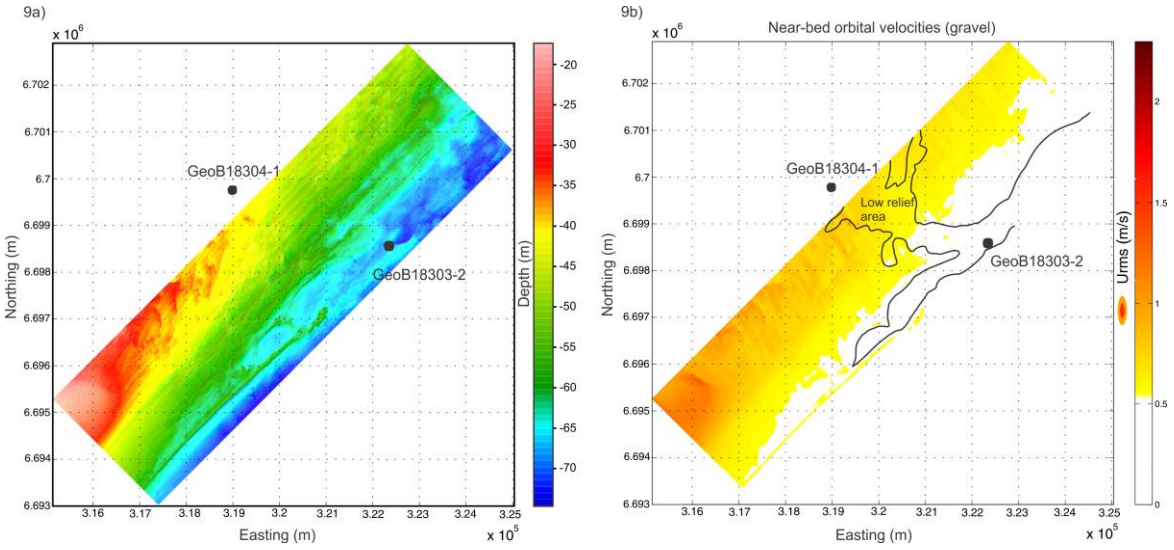

Figure 9. A regular structured grid with 5 meters depth resolution was used for representing the computational domain. a) The bathymetric grid representing the bottom conditions of the study area. b) Displays the modelled wave field near bottom orbital velocities, represented according to the threshold value for gravelly sediment mobility greater than 0.52 m/s for offshore boundary conditions for the March 2007 storm event (Hs- 8.5 m; Hmax-12.38 m; Tp- 16.6sec; θ- 147°). The line present represents the position of the old incised valley after Green et al (2013b).

CHAPTER 5

5.1. Discussion

5.1.1. Seismic and lithostratigraphic interpretations

Previous work by Green et al (2013a and b), revealed the presence of incised valleys on the Durban continental shelf. Core GeoB18303-2 intersected the uppermost horizons of one of these valleys, notably the incised valley fill of Unit A and revealed this to be comprised of organic-rich fine sand dating to 13 300 ± 70 cal yr BP deposited when former sea level was -75.5 m amsl ± 5 m (Vogel and Marais, 1971; Ramsey and Cooper, 2002). This is truncated by Surface i, which is interpreted as the tidal ravinement surface (tRS) in the upper valley fill. The geochemical signatures of the underlying Unit A (lithofacies 1) are marked by increased abundances of the terrigenous elements Si, Al and Fe, signifying a high abundance of terrestrial sediment supply to the system at the time of deposition, likely indicating a terrestrial sedimentary environment.

Sub-unit Ai overlies Surface i and consists of seaward prograding parallel reflectors and could be representative of a small ebb tide delta or a tidal bedform in the upper estuary system. Green et al (2013a) consider this valley to have transitioned to a lagoonal setting during a stillstand between 13 000 and 11 500 yr BP. It is likely this is a small progradational body within this lagoonal system that marks the general segmentation of the lagoonal system (cf. Green et al., 2013a). GeoB18303-2 intersected this unit (facies 5) in the more distal portions of the incised valley and reveal sedimentary and geochemical signatures consistent with a tidal type of deposit that coincide with this time (13 300 ± 70 cal yr BP to 11 690 ± 90 cal yr BP), when former sea levels were between -75.5 m amsl ± 5 m (Vogel and Marais, 1971) and -48 m amsl ± 3 m (Grobbler et al., 1988), respectively. These include coarser grain sizes and higher abundances of the marine elements such as Ca and Sr.

The upper portions of Unit A below Surface 1 were intersected in the proximal parts of the incised valley system by core GeoB18304-1 (at a depth of 38.2 m). Like the other core, these deposits show enrichment in the terrigenous elements (Fig. 7) and are capped by Surface 1. Surface 1 is a high amplitude reflector which occurs regionally

and caps the aeolianites/beachrock ridges, truncates the incised valley fills and underlies Unit B. This surface is the equivalent of the wave ravinement surface (WRS) and is marked by the presence of shell hash, pebbles and cobbles of aeolianite and beachrock derived from the aeolianite/beachrock ridges.

Unconformably overlying the WRS, is Unit B. Sub-unit B1, located between depths of 60 m and 80 m, has an internal configuration that consists of parallel reflectors which aggradationally onlap the subaerial WRS and the aeolianites/beachrock ridges. This geometry is consistent with that of transgressive sand sheets that have formed in a response to ongoing ravinement of the upper and middle shoreface during transgression eroding barrier, estuarine and relict sediment, transferring sediments seaward to offshore (e.g. Swift and Thorne, 1991; Posamentier and Allen, 1993; McBride et al., 2004). Posamentier and Allen (1993) inferred the underlying surface to represent the wave ravinement surface. The absence of this sand sheet at depths < 68 m can be attributed to the rapid sea-level rise (Broecker and van Donk, 1970) associated with the preservation of the barrier/aeolianite complex (Green et al., 2013a) and limited erosion. Numerous physical oceanographic studies on the erosive nature of high energy storm swell indicates that contemporary storm events support cross shelf sediment transport, resulting in the re-suspension of shelf sediment near the storm wave base and resultant offshore sediment transport (Wright et al., 1994; Harris and Wiberg, 2002). As such extreme storm events may have contributed to offshore sedimentation in conjunction with rapid sealevel rise associated with limited shelf sedimentation. This results in the offshore contribution of sediments to the sand sheets at depth. Pretorious et al (in press) consider these to be separated from the main shoreface sediment body by the first aeolianites/beachrock ridges that created a temporal disconnection between the migration of the shoreface and the more landward elements of the littoral system.

Sub-unit B2 consists of prograding, oblique parallel, seaward-dipping moderate amplitude reflectors which onlap and downlap the WRS. Field and Roy (1984) described comparable seismic units from a similarly steep, high-energy shoreface. These were formed during high energy events that resulted in the net seaward transport of sediments and deposition below wave base such as in this example.

Sub unit B3 onlaps surface 1 and the associated aeolianites/beachrock ridges. This unit occurs as a series of seaward thinning wedges of shelly sediment with notably irregular, wavy to chaotic high amplitude reflectors. The sedimentology of this unit is revealed by Core GeoB18303-2. The deposit comprises mudballs within a very coarse sand matrix. The mud ball internal layers date from when sea level was approximately 60 m below present, 10 010 ± 50 cal yr BP and 9 850 ± 50 cal yr BP, respectively. The outer layer of the upper mudball is dated at 3 835 ± 35 cal yr BP, giving the minimum age of this unit. Overall the geochemical signatures are dominantly marine, interspersed with minor terrestrial occurrences. This unit is interpreted as an aggradational high-energy lower shoreface deposit. The significance of this unit is discussed further in section 5.2.

Sub-unit B4 is present at ~ 60 to 16 m depths of and rests on the WRS in the proximal areas and comprises a set of progradational reflectors (Fig. 4). The corresponding lithofacies are a series of alternating deposits of coarse shelly material and medium sands dating from 6480 ± 40 cal yr BP to 4595 ± 35 cal yr BP (Tables 1 and 2), when sea level was approximately 0 m to 2.75 m amsl (Ramsey, 1995), respectively The coarser packages of facies 5 and 3 are characterised by higher abundances of the marine fraction elements, separated by finer material with a higher terrigenous elemental abundance in facies 2. Alternating fining upwards horizons displaying clear marine signatures interbedded with terrestrially derived material are often associated with high energy marine events (Morton et al., 2007; Goff et al., 2012). Unit B4 is thus interpreted as a high energy prograding portion of the lower shoreface.

Sub-unit B4 is toplapped by surface ii, a moderate amplitude surface present only at depths shallower than 40 m. There is no clear sedimentological expression of this layer in GeoB18304-1, however the surface is tentatively linked to the slight coarsening in the core at a depth of ~ 1 m. This is overlain by Sub-unit B5. Dates from 1.45 m and 0.25 m constrain the deposition of this Sub-unit to between 2845 ± 30 cal yr BP and 2 270 ± 30 cal yr BP deposited when sea level was near present day levels (Ramsey,1995). The contemporary storm wave regime has been assigned at ~ 30 m depth (Smith et al., 2010), just below which this Sub-unit occurs. The sandy nature of the unit and its position identify it as the contemporary lower shoreface of the study.

5.1.2. The significance of Sub-unit B3 and B4

Sub-unit B3, represented by the distal core GeoB18303-2, is characterised by the presence of mudballs of terrestrial origin, given by the high Ti abundances (Fig. 6b). These occur within a coarse grained shell hash with high marine elemental signatures. Mudballs (or peatballs) on the shelf are commonly found in storm-dominated shelf settings where the coastline is undergoing transgressive erosion (e.g. Yoo et al., 2014). These are related to the storm-driven erosion of muddy coastal/fluvial material and subsequent offshore transport by storm-return flows to below the storm wave base (Walker and Plint, 1992; Hampson and Storms, 2003). This paper considers the mud to be derived from an outcropping or subcropping source on the foreshore of the adjoining coastal plain. Such a scenario is occurring presently, whereby storm sculpting exposes laterally continuous mud layers along the shoreline of the study area (Cooper and Mason, 1986). The mudballs thus represent the transgressive erosion of terrestrial-sourced muds from the foreshore and subsequent deposition within the associated tempestite sequence in the lower shoreface (the coarse grained matrix of facies 4). It is notable that no further mudballs are encountered in the upper stratigraphy of either of the cores. The outer layer date of the mudball reflects the earliest point of deposition of this material on the shelf.

Sub-unit B4 comprises discrete sedimentary packages consisting of the coarsest fractions of the core material. These include alternating layers of terrestrial and marine provenance e.g. GeoB18304-1 (Fig. 5.2). The marine dominated shell and pebble hash horizons bear a strong resemblance to the deposits found by many authors associated with storm scour or “rippled scour depressions” found on the inner shelf (e.g. Murray and Thieler, 2004; Goff et al., 2005; Trembanis and Hume, 2011). The small scale fining upward packages that terminate with terrestrial element-rich sands is similar to the tempestite sedimentology described by Walker and Plint (1992). Sub-unit B4 is thus considered to comprise a series of storm-generated gravel/sand couplets.

5.1.3. Timing of storm induced events

Sub-units B3 and B4 and the storm intervals they record both span two distinct time periods. The more distally located storm deposits date from 10 680 ± 50 cal yr BP to 3 835 ± 35 cal yr BP and the more proximal from 6 480 ± 40 cal yr BP to 4 595 ± 35 cal yr BP. When placed within the context of palaeo-sea levels of the area, the older storms are associated with sea levels of ~ 30-40 m below mean sea level (Ramsay and Cooper, 2002), whereas the proximal group occurred when sea level was more precisely located between + 3 m and mean sea level (Ramsay, 1995; Ramsay and Cooper, 2002) (Fig. 3).

Lowered wave based consequent with a lowered sea-level framework may certainly have been responsible for the older and more distal storm deposits. The lowermost of these deposits dates to a point in time when global sea levels occupied depths of ~ 38 m (cf. Peltier and Fairbanks, 2006). Given the relatively small GIA for the east coast of South Africa (Milne and Mitrovica, 2008), it is reasonable to consider the Holocene sea level history of Durban to be similar to that of the eustatic sea level curve. It stands to reason that these deposits may have been related to a significantly lower wave base and the development of upper shoreface hosted rippled scour depressions. Sea level was likely too high for these deposits to represent back barrier-hosted washovers as the main barrier is situated at ~ 60 m depth.

The proximal horizons are of particular interest when examined in the context of contemporary shelf sediment mobility (and thus similar sea levels to those established for the cored deposits). The largest of the contemporary storms have had little to no effect on the movement or deposition of gravel on the shelf (Fig. 9). Similarly the overall smooth seafloor morphology of the lower shoreface (lack of scours etc.) reveals very little modern storm wave interaction with the seabed. Instead, the palaeo-storm deposits preserved in the lower shoreface point to a series of storms that occurred in the past that were of far greater magnitude than the largest storms of today.

5.1.4. Comparison with contemporary conditions

Previous studies on climatic factors controlling Holocene storm records in the Indian Ocean focus on contemporary climatic processes. Numerous studies suggest that sea surface temperature is a major contributor to periods of storminess and increased levels of rainfall experienced in the western Indian Ocean (Mutai et al., 1998; Nicholson, 1997; Ogallo et al., 1988; Cadet and Diehl, 1984). In particular, Webster et al (2005) show strong evidence that in the North Atlantic, increases in tropical cyclone intensity, duration and frequency are associated with strong warming periods and increased SST.

Kuhnert et al (2014) indicates the Holocene climate over the Indian Ocean is a result of various atmospheric and oceanic conditions, related closely to the Indian Ocean dipole (IOD). The IOD is an ocean/atmosphere phenomenon which forms as a result of changes in the sea surface temperatures (SST) in the equatorial region of the Indian Ocean. Negative IOD events result in higher rainfall over Western Indonesia (Saji et al., 1999; Webster et al., 1999; Yu and Rienecker, 1999; 2000, Abram et al., 2007) and drier conditions over East Africa (Webster et al., 1999), and positive IOD events are associated with increased rainfall (and by proxy increased storminess) over East Africa (Webster et al., 1999). Ding and Li, (2012) indicated that enhanced convection over the Indian Ocean is a response to the co-occurrence of an El Niño event and a positive IOD event. Large changes in the monsoon rainfall in the eastern Indian Ocean can be attributed to the occurrence of El Niño southern oscillation (ENSO) (Gadgil et al., 2004) and strong IOD events (Deshpande et al., 2014) which may act to increase SST and thus increase the likelihood for larger and more frequent tropical cyclones.

The proximal core that contained a record of events that occurred during contemporary sea levels reflects a record of intense storminess that affected the lower shoreface between 6 480 ± 40 cal yr BP to 4 595 ± 35 cal yr BP. This period of time is coincident with a strongly positive IOD state of the Indian Ocean resulting in arid conditions over the eastern Indian Ocean and increased precipitation over the western margin of the Indian Ocean when coupled with El Niño events (Wang et al., 2005; Fleitmann et al., 2007; Mohtadi et al., 2011). During this time period, a positive IOD (mean state) predominated, where SST warming in the western Indian Ocean, was coupled with cooling of SST's in the east (Abram et al., 2007). This dissertation thus proposes that

the storm horizons are linked to this major increase in mid Holocene SST and reflect a particularly aggressive period of storminess that has not been repeated since. This may be due to the later shift towards a stronger El Niño and a less prominent Eastern Indian Ocean monsoon since 3600 BP (Abram et al., 2007).

To date, this is the first study which has examined the palaeo-storm record from the western Indian Ocean. The majority of studies focusing on the 'mean-state' change of atmospheric circulation patterns and oceanic currents in the Indian Ocean, particularly those linked with global warming, recognise rapid warming of SST's in the west dominated by strong easterly winds and weakening of eastward oceanic currents along the equatorial Indian Ocean. It is widely accepted that these conditions promote the formation of positive IOD anomalies, facilitated by atmospheric and oceanic current reversals (Vecchi and Soden, 2007; Cai et al., 2013; Zheng et al., 2013). The consequence of global warming on climatic conditions associated with extreme IOD events is unknown. However, recent studies have focused on modelling IOD events with associated global warming and indicate an increase in the frequency of extreme positive IOD events with a projected increase in the recurrence interval, from one every 17.3 yrs to one every 6.3 yrs from the twentieth to twenty first century (Cai et al., 2014). Global warming therefore can be associated with an increase in positive IOD events affecting regions along the east African coast resulting in an increase in frequency in extreme events associated with weather and climate.

Changes in atmospheric circulation patterns and oceanic currents associated with global warming are thus likely to result in an increase in storminess as they promote the formation of positive IOD events. The magnitude of these events is largely unknown, however these changes are likely to promote prolonged positive IOD events. These events are likely to result in increased frequency of intense storminess and magnitude of storms affecting the east coast of South Africa.

CHAPTER 6

6.1 Conclusion

Ultra-high resolution seismic profiles show the presence of several packages of irregular, wavy to chaotic reflectors within the sedimentary package of the contemporary lower-shoreface. This package overlies an old incised valley of latest Pleistocene to early Holocene age.

Based on core data, the wavy to chaotic reflector packages are interpreted as comprising a variety of storm layers or tempestites. This is confirmed by their coarser grain sizes, dominance of shelly and pebbly debris and increased abundances in elements associated with marine influences. These are interposed with layers reflecting terrestrial processes, interpreted as fair-weather conditions.

These storm packages date from 6 480 ± 40 cal yr BP to 4 595 ± 35 cal yr BP in the proximal areas to 10 680 ± 50 cal yr BP to 3 835 ± 35 cal yr BP in the distal areas. The proximal areas experienced storm deposition during a period when sea level occupied a level similar to that of contemporary mean sea level. The distal storm packages represent a period when the sea level was substantially (~ 40 m) lower than present and are thus likely to coincide with lowered wave bases.

Contemporary bathymetry shows no scouring or storm impacts on the lower shoreface where the cores were taken. Modelling of the effects the largest recoded storm had on the lower shoreface show that the impacts in terms of sediment movement were minimal. It thus appears the 6 480 ± 40 cal yr BP to 4 595 ± 35 cal yr BP storm package represents an exceptionally stormy period.

This period of exceptional marine storminess is linked to a strongly positive Indian Ocean Dipole event that caused sea surface temperatures (SST's) to increase and prompted stronger, more intense and longer duration tropical cyclones to impact the Durban coastline.

This study shows for the first time the existence of an increased period of storminess in the Indian Ocean. It shows that Durban in particular is susceptible to warming SST's,

which are strongly related to positive IOD events. Changes in atmospheric circulation patterns and oceanic currents associated with global warming are likely to result in an increase in storminess as they promote the formation of such positive IOD phenomena.

References

Abram, N.J., Gagan, M.K., Liu, Z., Hantoro, W.S., McCulloch, M.T., Suwargadi, B.W., 2007. Seasonal characteristics of the Indian Ocean Dipole during the Holocene epoch. Nature 445(7125), 299-302.

Aigner, T., Reineck, H.E., 1982. Proximality trends in modern storm sands from the Helgoland Bight (North Sea) and their implications for basin analysis. Senckenbergiana Maritima 14(5), 183-215.

Arz, J.A., Arenillas, I., Soria, A. R., Alegret, L., Grajales-Nishimura, J. M., Liesa, C.L., Meléndez, A. Molina, E., and Rosales, M. C., 2001. Micropaleontology and Sedimentology of the Cretaceous/Tertiary boundary at La Ceiba (Mexico): impact-generated sediment gravity flows. Journal of South American Earth Sciences 14(5), 505-519.

Arz, H.W., Pätzold, J., Müller, P.J., Moammar, M.O., 2003. Influence of Northern Hemisphere climate and global sea level rise on the Red Sea marine environment during termination I. Paleoceanography 18(2), 1053.

Backstrom, J.T., Jackson, D.W.T., Cooper, J.A.G., 2009. Shoreface morphodynamics of a high-energy, steep and geologically-constrained shoreline segment in Northern Ireland. Marine Geology 257, 94-106.

Badenhorst, P., Cooper, J.A.G., Crowther, J., Gonsalves, J., Grobler, N.A., Illenberger, W.K., Laubscher, W.I., Mason, T.R., Moller, J.P., Perry, J.E., Reddering, J.S.V., Van der Merwe, L., 1989. Survey of September 1987 Natal floods. Foundation for Research Development, CSIR, Pretoria. South African National Scientific Programmes. Report 164, 137 pp.

Belknap, D.F., Kraft, J.C., 1981. Preservation potential of transgressive coastal lithosomes on the US Atlantic shelf. Marine Geology 42, 429-442.

Bentley, S.J., Keen, T.R., Blain, C.A., Vaughan, W.C., 2002. The origin and preservation of a major hurricane event bed in the northern Gulf of Mexico: Hurricane Camille, 1969. Marine Geology 186(3-4), 423-446.

Berg, R.R., Davies, D.K., 1968. Origin of lower Cretaceous Muddy Sandstone at Bell Creek Field, Montana. American Association of Petroleum Geologist Bulletin 52(20), 1888-1898.

Birch, G.F., 1996. Quaternary Sedimentation off the East Coast of southern Africa (Cape Padrone to Cape Vidal). Bulletin of the Geological Survey of South Africa, Council for Geoscience 118, 55 pp.

Booij, N., Ris, R.C., Holthuijsen, L.H., 1999. A third-generation wave model for coastal regions-1. Model description and validation. Journal of Geophysical Research: Oceans 104(C4), 7649–7666.

Bridges, P.H., 1976. Lower Silurian transgressive barrier islands, southwest Wales. Sedimentology 23(3), 347-362.

Broad, D.S., Jungslager, E.H.A., McLachlan, I.R., Roux, J., 2006. Offshore Mesozoic Basins. In: Johnson, M.R., Anhaeusser, C.R., Thomas, R.J. (Eds), The Geology of South Africa. Geological Society of South Africa, Johannesburg and Council for Geoscience, Pretoria. pp. 553-571.

Broeker, W, S., van Donk, J., 1970. Insolation changes, ice volumes and the O^{18} record in deep-sea cores. Reviews of Geophysics and Space Physics 8(1), 169-198.

Browne, I. 1994. Seismic stratigraphy and relict coastal sediments off the east coast of Australia. Marine Geology 122 (1-2), 81-107.

Cadet, D. L., Diehl, B., 1984. Interannual variability of the surface field over the Indian Ocean during the recent decades. Monthly Weather Review 112, 1921-1935.

Cai, W., Zheng, X.T., Weller, E., Collins, M., Cowan, T., Lengaigne, M., Yu, W., Yamagata, T., 2013. Projected response of the Indian Ocean Dipole to greenhouse warming. National Geoscience 6, 999-1007.

Cai, W., Santoso, A., Wang, G., Weller, E., Wu, L., Ashok, K., Masumoto, Y., Yamagata, T., 2014. Increased frequency of extreme Indian Ocean Dipole events due to greenhouse warming. Nature 510, 254-258.

Calvert, S.E., Pedersen, T.F., 2007. Elemental proxies for palaeoclimatic and palaeoceanographic variability in marine sediments: interpretation and application. In Hillaire-Marcel, C., de Vernal, A (ed.), developments in Marine Geology. Elsevier, Oxford 1, 567-644.

Camoin, G.F., Montaggioni, L.F., Braithwaite, C.J.R., 2004. Late Glacial to post glacial sea levels in the western Indian Ocean. Marine Geology 206(1), 119-146.

Cawthra, H.C., Uken, R., Ovechkina, M.N., 2012. New insights into the geological evolution of the Durban Bluff and Adjacent Blood Reef, South Africa. South African Journal of Geology 115(3), 291-308.

Collins, E.S., Scott, D.B., Gayes, P.T., 1999. Hurricane records on the South Carolina coast: Can they be detected in the sediment record? Quaternary International 56(1), 15-26.

Cooper, J.A.G., Mason, T., 1986. Subaerial washover fans in the Beachwood mangrove area, Durban. Department of Geology and Applied Geology, University of Natal, Durban, Sedimentation in Estuaries and Lagoons, Report 1, 23 pp.

Cooper M.R., Greyling E.H., 1996. Stratigraphy and palaeontology of a temporary exposure of the Mzamba Formation (Upper Cretaceous, Lower Campanian) in the Eastern Cape, South Africa. Durban Museum Novitates 21, 11-24.

Corbella, S., Stretch, D.D., 2012. The wave climate on the KwaZulu-Natal coast of South Africa. Journal of the South African Institution of Civil Engineering 54(2), 45-54.

Curray, J. R., 1964. Transgressions and regressions. In: Miller, R. L. (Ed.), Papers in marine geology -Shepard commemorative volume: New York, Macmillan Co., pp. 175-203.

Davis, R.A., Kuhn, B.J., 1985. Origin and development of Anclote Key, west-peninsular, Florida. Marine Geology 63(1-4), 153-171.

Davis, R.A., Jr., Knowles, S.C., Bland, M.C., 1989b. Role of hurricanes in the Holocene stratigraphy of estuaries: examples from the Gulf coast of Florida. Journal of Sedimentary Petrology 59, 1052-1061.

Davies, D.K., Ethridge, F.G., Berg, R.R., 1971. Recognition of barrier environments. American Association of Petroleum Geologists Bulletin 55(4), 550-565.

Deery, J.R., Howard, J.D., 1977. Origin and character of washover fans on the Georgia Coast, U.S.A. Gulf Coast Association of Geological Societies Transactions 27, 259-271.

Delany, C., Devoy, R., 1995. Evidence from sites in western Ireland of late Holocene changes in coastal environments. Marine Geology 124(1-4), 273-287.

Deshpande, A., Chowdary, J.S., Gnanaseelan, C., 2014. Role of thermocline SST coupling in the evolution of IOD events and their regional impacts. Climate Dynamics 43(1), 163-174.

Dingle, R.V., Siesser, W.G., Newton, A.R., 1983. Mesozoic and Tertiary Geology of Southern Africa. Balkema, Rotterdam, 375 pp.

Donnelly, J.P., Bryant, S.S., Butler, J., Dowling, J., Fan, L., Hausmann, N., Newby, P., Shuman, B., Stern, J., Westover, K., Webb III, T., 2001a. 700 yr sedimentary record of intense hurricane landfalls in southern New England. Geological Society of America Bulletin 113(6), 714-727.

Donnelly, J.P., Roll, S., Wengren, M., Butler, J., Lederer, R., Webb III, T., (2001b). Sedimentary evidence of intense hurricane strikes from New Jersey. Geological Society of America 29(7), 615-618.

Donnelly, J.P., Woodruffe, J., 2007. Intense hurricane activity over the past 5000 years controlled by El Nino and the West African Monsoon. Nature 447(7143), 465-468.

Dott, R.H., Bourgeois, J., 1982. Hummocky stratification: Significance of its variable bedding sequences. Geological Society of America Bulletin 93(8), 663-680.

Ehlers, J., Nagorny, K., Schmidt, P., Stieve, B., Zietlow, K., 1993. Storm surge deposits in North Sea salt marshes dated by 134Cs and 137Cs determination. Journal of Coastal Research 9(3), 698-701.

Field, M.E., Roy, P.S., 1984. Offshore transport and sand-body formation: evidence from a steep, high-energy shoreface, southeastern Australia. Journal of Sedimentary Petrology 54(4), 1292–1302.

Flemming, B.W., 1980. Sand transport and bedform patterns on the continental shelf between Durban and Port Elizabeth (Southeast African continental margin). Sedimentary Geology 26(1-3), 179-205.

Flemming, B.W., 1981. Factors controlling shelf sediment dispersal along the southeast African continental margin. Marine Geology 42(1-4), 259-277.

Fleitmann, D., Burns, S.J., Mangini, A., Mudelsee, M., Kramers, J., Villa, I., Neff, U., Al Subbary, A.A., Buettner, A., Hippler, D., Matter, A., 2007. Holocene ITCZ and Indian monsoon dynamics recorded in stalagmites from Oman and Yemen (Socotra). Quaternary Science Review 26(1-2), 170-188.

Forbes, D.L., Parkes, G.S., Manson, G.K., Ketch,L.A., 2004. Storms and shoreline retreat in the southern Gulf of St.Lawrence. Marine Geology 210(1-4), 169–204.

Gadgil, S., Vinayachandran, P.N., Francis, P.A., Gadgil, S., 2004. Extremes of the Indian summer monsoon rainfall, ENSO and equatorial Indian Ocean oscillation. Geophysical Research Letters 31(12), L12213. DOI: 10.1029/2004GL019733.

Gebhardt, H., Sarnthein, M., Grootes, P.M., Kiefer, T., Kuehn, H., Schmieder, F., Rohl, U., 2008. Paleonutrient and productivity records from the subarctic North Pacific for Pleistocene glacial terminations I to V. Paleoceanography, 23, PA4212. DOI: 10.1029/2007PA001513.

Goff, J.R., McFadgen, B.G., Chague´-Goff, C., 2004. Sedimentary differences between the 2002 Easter storm and the 15th-century Okoropunga tsunami, southeastern North Island, NewZealand. Marine Geology 204(1-2), 235-250.

Goff, J., Chagué-Goff, C., Nichol, S., Jaffe, B., Dominey-Howes, D., 2012. Progress in palaeotsunami research. Sedimentary Geology, 243–244: 70–88. DOI:10.1016/j.sedgeo.2011.11.002.

Goff, J.A., Mayer, L.A., Traykovski, P., Buynevich, I., Wilkens, R., Raymond, R., Glang, G., Evans, R.L., Olson, H., Jenkins, C., 2005. Detailed investigation of sorted bedforms, or "rippled scour depressions," within the Martha's Vineyard Coastal Observatory, Massachusetts. Continental Shelf Research 25(4), 461-484. DOI: 10.1016/j.csr.2004.09.019

Goodlad, S.W., 1986. Tectonic and sedimentary history of the mid-Natal Valley (SW Indian Ocean). Bulletin of the Joint Geological Survey/ University of Cape Town. Marine Geoscience Unit 15, 415 pp.

Green, A.N., 2009a. Sediment dynamics on the narrow, canyon-incised and current-swept shelf of the northern KwaZulu-Natal continental shelf, South Africa. Geo-Marine Letters 29(4), 201-219.

Green, A.N., 2009b. Palaeo-drainage, incised valley fills and transgressive systems tract sedimentation of the northern KwaZulu-Natal continental shelf, South Africa, SW Indian Ocean. Marine Geology 263(1), 46-63.

Green, A., Garlick, G.L., 2011. A sequence stratigraphic framework for a narrow, current-swept continental shelf: The Durban Bight, central KwaZulu-Natal, South Africa. Journal of African Earth Sciences 60(5), 303-314.

Green, A.N., Smith, A.M. (2012). Can ancient shelf sand ridges be mistaken for Gilbert-type deltas? Examples from the Vryheid Formation, Ecca Group, KwaZulu-Natal, South Africa. Journal of African Earth Science 76, 27-33.

Green, A., Leuci, R., Thackeray, Z., Vella, G., 2012a. Number One Reef: An overstepped segmented lagoon complex on the KwaZulu-Natal continental shelf. South African Journal of Science 108(7-8), 113-118. DOI: 10.4102/sajs. v108i7/8.969.

Green, A., Ovechkina, M.N., Mostovski, M.B., 2012b. Late Holocene shoreface evolution of the wave dominated Durban Bight, KwaZulu-Natal, South Africa: A mixed storm and current driven system. Continental Shelf Research 49, 56-64.

Green, A. Dladla, N., Garlick, L., 2013a. Spatial and temporal variations in incised valley systems from the Durban continental shelf, KwaZulu-Natal, South Africa. Marine Geology 335, 148-161.

Green, A.N., Cooper, J.A.G., Leuci, R., Thackeray, Z., 2013b. Formation and preservation of an overstepped segmented lagoon complex on a high-energy continental shelf. Sedimentology 60(6), 1755-1768. DOI: 10.1111/sed.12054.

Green, A.N., Cooper, J.A.G., Salzmann, L., 2014. Geomorphic and stratigraphic signals of postglacial meltwater pulses on continental shelves. Geology 42(2), 151-154.

Grützner, J., Rebesco, M.A., Cooper, A.K., Forsberg, C.G., Kryc, K.A., Wefer, G., 2003. Evidence for orbitally controlled size variations of the East Antarctic Ice Sheet during the late Miocene. Geology 31(9), 777-780.

Guastella, L.A. and Rossouw, J., 2009. Coastal Vulnerability: Are Coastal Storms Increasing in Frequency and Intensity Along the South African Coast? International Multi-Purpose Reef Conference (Jeffery's Bay, South Africa), p10.

Guillen, J., Camp, J., Palanques, A., 1994. Short-time evolution of a microtidal barrier-lagoon system affected by storm and overwashing: the Trabucador Bar Ebro Delta, NW Mediterranean. Zeitschrift für Geomorphologie 38(3), 267-281.

Harris, T.F.W., 1978. Review of coastal currents in Southern African waters. South African National Scientific Programmes Report, Council for Scientific and Industrial Research 30, 103 pp.

Harris, C.K., Wiberg, P.L., 2002. Across-shelf sediment transport: interactions between suspended sediment and bed sediment. Journal of Geophysical Research 107 (C1). DOI: 10.1029/2000JC000634.

Hampson, G. J., Storms, J. E. A., 2003. Geomorphological and sequence stratigraphic variability in wave-dominated, shoreface-shelf parasequences. Sedimentology 50(4), 667-701.

Hayes, M.O., 1967. Hurricanes as Geological Agents: Case Studies of Hurricanes Carla, 1961, and Cindy, 1963. University of Texas. Bureau of Economic Geology. Report 61, 54pp.

Hirschboeck, K.K., 1987. Catastrophic flooding and atmospheric circulation patterns. In: Mayer, L., Nash, D. (Eds.), Catastrophic Flooding. Allen and Unwin, Boston, p. 23-56.

Holthuijsen, LH., 2007. Waves in Oceanic and Coastal Waters. Cambridge University Press: Cambridge.

Jury, M.R., Melice, J.L., 2000. Analysis of Durban rainfall and Nile river flow 1871–1999. Theoretical and Applied Climatology 67(3), 161-169.

Keen, T.R., Bentley, S.J., Vaughan, W.C., Blain,C.A., 2004. The generation and preservation of multiple hurricane beds in the northern Gulf of Mexico. Marine Geology 210(1-4), 79–105.

Keen, T.R., Slingerland, R.L.,Bentley, S.L., Furukawa, Y., Teague, W.J., 2012. Sediment transport on continental shelves: storm bed formation and preservation in heterogeneous sediments. International Association of Sedimentologists. Special Publication 44, 295-310.

Kelley, J.T., Belknap, D.F., Claesson, S., 2010. Drowned coastal deposits with associated archaeological remains from a sea-level “slowstand”: northwestern Gulf of Maine, USA. Geology 38(8), 695-698. DOI: 10.1130/G31002.1.

Kochel, R.C., Dolan, R., 1986. The relative role of overwash on a mid-Atlantic coast barrier island. Journal of Geology 94, 902-906.

Komar, P.D., Miller, M.C., 1974. Sediment threshold under oscillatory waves. Proceedings of the 14th International Conference on Coastal Engineering. American Society of Civil Engineers1, 756-775.

Kennett, J. P., 1982. Marine Geology. Prentice Hall, Englewood Cliffs, New Jersey, 813 pp.

Komatsubara, J., Fujiwara, O., Takada, K., Sawai, Y., Aung, T.T., Kamataki, T., 2008. Historical tsunamis and storms recorded in a coastal lowland, Shizuoka Prefecture, along the Pacific Coast of Japan. Sedimentology 55(6), 1703-1716.

Kortekaas, S., Dawson, A.G., 2007. Distinguishing tsunami and storm deposits: An example from Martinhal, SW Portugal. Sedimentary Geology 200(3-4), 208-221.

Kuhlmann, H., Meggers, H., Freudenthal, T., Wefer, G., 2004. The transition of the monsoonal and the N Atlantic climate system off NW Africa during the Holocene. Geophysical Research Letters 31, L22204. DOI: 10.1029/2004GL021267.

Kuhnert, H., Kuhlmann, H., Mohtadi, M., Meggers, H., Baumann, K.-H., P€atzold, J., 2014. Holocene tropical western Indian Ocean sea surface temperatures in covariation with climatic changes in the Indonesian region. Paleoceanography 29, 423-437. DOI: 10.1002/2013PA002555.

Kraft J.C., Chrzastowski M.J. 1978. Coastal Stratigraphic Sequences. In Davis R.A. Jr.(eds.), Coastal Sedimentary Environments. 625-664.

Leatherman, S.P., 1977. Quantification of overwash processes. Ph.D. dissertation, University of Virginia, 245 pp.

Leatherman, S.P., Williams, A.T., 1977. Lateral textural grading in overwash sediments. Earth Surface Processes and Landforms 2(4), 333-341.

Leatherman, S.P., Williams, A.T., 1983. Vertical sedimentation units in a barrier island washover fan. Earth Surface Processes and Landforms 8(2), 141-150.

Liu, K., Fearn, M.L., 1993. Lake-sediment record of late Holocene hurricane activities from coastal Alabama. Geology 21(9), 793-796.

Liu, K.B., Fearn, M.L., 2000. Reconstruction of prehistoric landfall frequencies of catastrophic hurricanes in northwestern Florida from lake sediment records. Quaternary Research 54 (2), 238-245.

Loureiro, C., Ferreira, Ó., Cooper, J.A.G., 2012. Extreme erosion on high-energy embayed beaches: influence of megarips and storm grouping. Geomorphology 139-140, 155-171.

Loureiro, C., Ferreira, Ó., Cooper, J.A.G., 2013. Applicability of parametric beach morphodynamic state classification on embayed beaches. Marine Geology 346, 153-164.

Martin, A.K., Flemming, B.W., 1988. Physiography, structure and geological evolution of the Natal Continental Shelf. In Schumann, E.H. (Ed.), Coastal Ocean Studies off Natal, South Africa. Springer-Verlag, New York. DOI: 10.1029/LN026p0011.

Masselink, G., van Heteren, S., 2014. Response of wave-dominated and mixed-energy barriers to storms. Marine Geology, 352, 321-347. DOI: 10.1016/j.margeo.2013.11.004.

McBride, R.A., Moslow, T.F., Roberts, H.H., Diecchio, R.J., 2004. Late Quaternary geology of the northeast Gulf of Mexico shelf: Sedimentology, depositional history and ancient analogues of a major shelf sand sheet of the modern transgressive systems tract. In Anderson, J.B., Fillon F.H, (ed.), Late Quaternary stratigraphic evolution of the Northern Gulf of Mexico margin. Society of Sedimentary Geology Special Publication 79, 55-83.

McCarthy, M.J., 1967. Stratigraphic and sedimentological evidence from the Durban region of major sea level movements since the Late Tertiary. Transactions of the Geological Society of South Africa 70, 135-165.

McMillan, I.K., 2003. Foraminiferally defined biostratigraphic episodes and sedimentation pattern of the Cretaceous drift succession (early Barremian to Late

Maastrichtian) in several basins on the South African and southern Namibian continental margin. South African Journal of Science 99, 537-576.

Mellett, C.L., Hodgson, D.M., Lang, A., Mauz, B., Selby, I., Plater, A.J. 2012. Preservation of a drowned gravel barrier complex: A landscape evolution study from the north-eastern English Channel. Marine Geology 315–318, 115–131.

Milne, G. A., Mitrovica, J. X., 2008. Searching for eustasy in deglacial sea-level histories. Quaternary Science Reviews 27(25-26), 2292-2302.

Moes, H., Rossouw, M., 2008. Considerations for the utilization of wave power around South Africa. Workshop on Ocean Energy, Centre for Renewable and Sustainable Energy Studies, Stellenbosch, 21, February 2008, Abstracts.

Mohtadi, M., Oppo, D.W., Steinke, S., Stuut, J.B.W., De Pol Holz, R., Hebbeln, D., Luckge, A., 2011. Glacial to Holocene swings of the Australian-Indonesian monsoon. Nature Geoscience 4, 540-544.

Morton, R.A., 1979. Large-scale rhomboid bed forms and sedimentary structures associated with hurricane washover. Sedimentology 25(2), 183-204

Morton, R.A., 1981. Formation of storm deposits by wind-forced currents in the Gulf of Mexico and the North Sea. In Nio, S.D., Shuttenhelmand, R.T.E., van Weering, T.C.E. (Ed.), Holocene Marine Sedimentation in the North Sea Basin. International Association of Sedimentology Special Publication 5, 385-396.

Morton, R.A., Gelfenbaum, G., Jaffe, B.E., 2007. Physical criteria for distinguishing sandy tsunami and storm deposits using modern examples. Sedimentary Geology 200(3), 184-207.

Mucina, L., Scott-Shaw, C.R., Rutherford, M.C., Kemp, K.G.T., Matthews, W.S., Powrie, L.W., Hoare, D.B., 2006. Indian Ocean coastal belt. In: Mucina, L., Rutherford, M.C. (Eds.), The Vegetation of South Africa, Lesotho and Swaziland: Strelitzia 19, South African National Biodiversity Institute, Pretoria, 569-583.

Murray, A.B., Thieler, E.R., 2004. A new hypothesis and exploratory model for the formation of large-scale inner-shelf sediment sorting and "rippled scour depressions". Continental Shelf Research 24(3), 295-315.

Mutai, C. C., M. N. Ward, and A. W. Colman, 1998. Towards the prediction to the East Africa short rains based on sea surface temperature–atmosphere coupling. International Journal of Climatology 18(9), 975-997.

Nanayama, F., Shigeno, K., Satake, K., Shimokawa, K., Koitabashi, S., Miyasaka, S., Ishii, M., 2000. Sedimentary differences between the 1993 Hokkaido-nansei-oki tsunami and the 1959 Miyakojima Typhoon at Taisei, south western Hokkaido, northern Japan. Sedimentary Geology 135(1-4), 255-264.

Nicholson, S. E., 1997: An analysis of the ENSO signal in the tropical Atlantic and western Indian Oceans. International Journal of Climatology 17(4), 345-375.

Oertel, C.F., 1975. Ebb tidal deltas of Georgia estuaries: In Cronin, L.E., (ed.), Estuarine Research. New York, Academic Press II, 587 pp.

Ogallo, L. J., J. E. Janowiak, and M. S. Halpert, 1988: Teleconnection between seasonal rainfall over East Africa and global sea surface temperature anomalies. Journal of the Meteoric Society of Japan 66(6), 807-821.

Partridge, T.C., Botha, G.A., Haddon, I.G., 2006. Cenozoic deposits of the interior. In: Johnson, M.R., Anhaeusser, C.R., Thomas, R.J. (Eds.), The Geology of South Africa. Geological Society of South Africa, Johannesburg/Council for Geoscience, Pretoria, South Africa, 585-604.

Partridge, T.C., Maud, R.R., 1987. Geomorphic evolution of southern Africa since the Mesozoic. South African Journal of Geology 90, 179-208.

Pearce, A.F., 1977. Some features of the upper 500 m of the Agulhas Current. Journal of Marine Research 35(4), 731-753.

Peltier, W.R., Fairbanks, R.G., 2006. Global glacial ice volume and Last Glacial Maximum duration from an extended Barbados sea level record. Quaternary Science Review 25(23-24), 3322–3337.

Percival, C.J., 1992. The Harthope Ganister: a transgressive barrier island to shallow-marine sand-ridge from the Namurian of Northern England. Journal of Sedimentary Research 62(3), 442-454.

Phantuwongraj, S., Choowong, M., 2012. Tsunamis versus storm deposits from Thailand. Natural Hazards 63(1), 31-50.

Posamantier, H.W., AlIen, G.P., 1993. Variability of the sequence stratigraphic model: effects of local basin factors. Sedimentary Geology 86(1-2), 91-109.

Pretorius, L.P., Green, A.N., Cooper, J.A.G., 2016. Submerged shoreline preservation and ravinement during rapid post glacial sea-level rise and subsequent slowstand. Bulletin of the Geological Society of America.

Psuty, N.P., 1986. Holocene sea level in New Jersey. Physical Geography 7(2), 156-167.

Rampino, M.R., Sanders, J.E., 1980. Holocene transgression in South-central Long Island, New York. Journal of Sedimentary Research 50(4), 1063-1079.

Ramsay, P.J., 1994. Marine geology of the Sodwana Bay shelf, southeast Africa. Marine Geology 120(3-4), 225-247.

Ramsay, P.J., 1995. 9000 years of sea-level change along the southern African Coastline. Quaternary International 31, 71-75.

Ramsay, P.J., Cooper, J.A.G., 2002. Late Quaternary sea-level change in South Africa. Quaternary Research 57(1), 82-90.

Reinson, G.E., 1992. Trangressive barrier island and estuarine systems. In: Walker, R.G., James, N.P. (Eds.), Facies Models: Responses to Sea-Level Change. Geological Association of Canada, Sittsville, Ontario, 179-195.

Ris, R.C., Holthuijsen, L.H., Booij, N., 1999. A third-generation wave model for coastal regions: 2. Verification. Journal of Geophysical Research 104(C4), 7667-7681.

Ritchie, W., Penland, S., 1988. Rapid dune changes associated with overwash processes on the deltaic coast of South Louisiana. Marine Geology 81(1-4), 97-122.

Roberts, D.L., Botha, G.A., Maud R.R., Pether, J., 2006. Coastal Cenozoic deposits. In: Johnson, M.R., Anhaeusser, C.R., Thomas, R.J. (Eds), The Geology of South Africa. Geological Society of South Africa, Johannesburg/Council for Geoscience, Pretoria, South Africa, 605-628.

Romero, O.E., Kim, J.H., Donner., 2008. Submillennial to millennial variability of diatom production off Mauritania, NW Africa, during the last glacial cycle. Paleoceanography 23(3), PA3218. DOI: 10.1029/2008PA001601.

van Rooij, D., Blamart, D., Richter, T., Wheeler, A., Kozachenko, M., Henriet, J.P., 2007. Quaternary sediment dynamics in the Belgica mound province, Porcupine Seabight: ice-rafting events and contour current processes. International Journal of Earth Sciences 96(1), 121-140.

de Ruijter, W. P. M., van Leeuwen, P. J., Lutjeharms, J. R. E., 1999. Generation and evolution of Natal Pulses: solitary meanders in the Agulhas Current. Journal Physical Oceanography 29(12), 3043-3055. DOI: 10.1175/1520-0485(1999)029<3043:GAEONP>2.0.CO;2.

Saji, N.H., Goswami, B.N., Vinayachandran, P.N., Yamagata, T., 1999. A dipole mode in the tropical Indian Ocean. Nature 401, 360-363.

Salzmann, L., Green, A.N., 2012. Boulder emplacement on a tectonically stable, wave dominated coastline, Mission Rocks, KwaZulu-Natal, South Africa. Marine Geology 323-325, 95-106.

Schefuß, E., Kuhlmann, H., Mollenhauer, G., Prange, M., Pätzold, J., 2011. Forcing of wet phases in southeast Africa over the past 17 000 years. Nature 480(7378), 509-512.

Schumann, E.H., 1987. The coastal ocean off the east coast of South Africa. Transactions of the Royal Society of South Africa 46(3), 215-229. DOI: 10.1080/00359198709520125.

Schwartz, R.K., 1975. Nature and genesis of some storm washover deposits. U.S. Army Corporation of Engineers. Coastal Engineering Research Centre. Technical Memorandum 61, 69 pp.

Shaw, J., 2005. Geomorphic evidence of postglacial terrestrial environments on Atlantic Canadian continental shelves. Geographie Physique et Quaternaire 59 (2-3), 141-154.

Shaw, J., Fader, G.B., Taylor, R.B., 2009. Submerged early Holocene coastal and terrestrial landforms on the inner shelves of Atlantic Canada. Quaternary International 206 (1-2), 24-34

Shepard, F.P., 1963. Submarine Geology. Harper and Row, New York, 557 pp.

Shinn, E.A., Steinen, R.P., Dill, R.F., Major, R., 1993. Lime-mud layers in high-energy tidal channels: A record of hurricane deposition. Geology 21(7), 303-306.

Simms, A.R., Lambeck, K., Purcell, A., Anderson, J.B., Rodrigues, A.B., 2007. Sea-level history of the Gulf of Mexico since the last glacial maximum with implications for the melting history of the Laurentide Ice Sheet. Quaternary Science Review 26(7), 920-940.

Smith, A.M., Mather, A.A,, Bundy, S.C., Cooper, J.A.G., Guastella, L.A., Ramsay, P.J., Theron, A., 2010. Contrasting styles of swell-driven coastal erosion: examples from KwaZulu-Natal, South Africa. Geological Magazine, 147(6), 940-953.

Snedden, J.W., Nummedal, D., Amos, A. F. (1988) Storm- and fair-weather combined flow on the central Texas continental shelf. Journal of Sedimentary Petrology 58(4), 580-595.

Snedden, J.W., Nummedal, D., 1990. Coherence of surf zone and shelf current flow on the Texas (USA) coastal margin: Implications for interpretation of paleo-current measurements in ancient coastal sequences. Sedimentary Geology 67(3), 221-236.

Snedden, J.W., Tillman, R.W., Culver, S.J., 2011. Genesis and evolution of a mid-shelf, storm-built sand ridge, New Jersey continental shelf, U.S.A. Journal of Sedimentary Research 81(7), 534-552.

Soulsby, R., 1997. Dynamics of Marine Sands: A Manual for Practical Applications. Thomas Telford: London. 249 pp.

Stapor, F.W., 1991. Barrier Island Progradation and Holocene Sealevel History in Southwest Florida. Journal of Coastal Research 7(3), 815-838.

Storms, J.E.A., Swift, D.J.P., 2003. Shallow-marine sequences as the building blocks of stratigraphy: insights from numerical modelling. Basin Research 15(3), 287-303.

Swift, D.J.P., 1968. Coastal erosion and transgressive stratigraphy. Journal of Geology 76(4), 444-456.

Swift, D.J.P., Phillips, S., Thorne, J.A., 1991. Sedimentation on continental margins, V: parasequences. In: Swift, D.J.P., Oertel, G.F., Tillman, R.W., Thorne, J.A. (Eds.), Shelf sand and sandstone bodies- geometry. Facies and Sequence Stratigraphy. International Association of Sedimentologists Special Publication, 14, 153-187.

Swift, D.J.P.,Moslow, T.F., 1982. Holocene transgression in South-central Long Island, New York; discussion. Journal of Sedimentary Research 52 (3), 1014–1019.

Swift, D.J.P., Thorne, J.A., 1991. Sedimentation on continental margins. Part I- A general model for shelf sedimentation. In Swift, D. J. P. (eds.), Shelf sand and sandstone bodies: Geometry, facies and sequence stratigraphy. International Association of Sedimentologists Special Publication 14, 3-31.

Switzer, A.D., Jones, B.G., 2008a. Large-scale washover sedimentation in a freshwater lagoon from the southeast Australian coast: sea-level change, tsunami or exceptionally large storm? The Holocene 18(5), 787-803.

Theron, A.K., Rossouw, M., Barwell, L., Maherry, A., Diedericks, G.P.J., de Wet, P., 2010. Quantification of risks to coastal areas and development: wave run-up and erosion. Science Real and Relevant Conference 2010. 16 pp.

Timmons, E.A., Rodriguez, A.B., Mattheus, C.R., DeWitt, R., 2010. Transition of a regressive to a transgressive barrier island due to back-barrier erosion, increased storminess, and low sediment supply: Bogue Banks, North Carolina, USA. Marine Geology 278 (1–4), 100–114.

Trembanis, A. C., T. M. Hume., 2011. Sorted bedforms on the inner shelf off northeastern New Zealand: Spatiotemporal relationships and potential paleo-environmental implications, Geo Marine Letters 31(3), 203-214. DOI: 10.1007/s00367-010-0225-8.

Tuttle, M.P., Ruffman, A., Anderson, T., Jeter, H., 2004. Distinguishing tsunami and storm deposits in eastern North America: The 1929 Grand Banks tsunami versus the 1991 Halloween storm. Seismological Research Letters 75, 117–131.

Tyson, P.D., 1986. Climate Change and Variability in Southern Africa, Cape Town. Oxford University Press, 220 pp.

Vecchi, G. A., Soden, B. J., 2007. Global warming and the weakening of the tropical circulation. Journal of Climatology 20(17), 4316-4340.

Vidal, L., Bickert, T., Wefer, G., Röhl, U., 2002. Late Miocene stable isotope stratigraphy of SE Atlantic ODP Site 1085: relation to Messinian events. Marine Geology 180(1-4), 71-85. DOI: 10.1016/S00253227(01)00206-7.

Vogt, C., Lauterjung, J., Fischer, R.X., 2002. Investigation of the clay fraction (<2 µm) of the clay mineral society reference clays. Clay and Clay Minerals 50(3), 388-400. DOI: 10.1346/000986002760833765.

Walker, R.G., Plint, A.G., 1992. Wave- and storm-dominated shallow marine systems. In Walker, R.G., and James, N.P., (eds). Facies models: response to sea-level changes. St. John's, Newfoundland, Canada, Geological Association of Canada, 219-238.

Wang, Y., Cheng, H., Edwards, R.L., He, Y., Kong, X., An, Z., Wu, J., Kelly, M.J., Dykoski, C.A., Li, X., 2005. The Holocene Asian Monsoon: links to solar changes and North Atlantic climate. Science 308(5723), 854-857. DOI: 10.1126/science.1106296.

Webster, P.J., Moore, A.M., Loschnigg, J.P., Leben, R.R., 1999. Coupled ocean-atmosphere dynamics in the Indian Ocean during 1997-98. Nature 401, 356-360. DOI: 10.1038/43848.

Webster, P. J., Holland, G. J., Curry, J. A., Chang, H.R., 2005. Changes in Tropical Cyclone Number, Duration, and Intensity in a Warming Environment, Science, 309(5742), 1844-1846. DOI: 10.1126/ science.1116448.

Willis, A.J., Moslow, T.F., 1994. Stratigraphic setting of transgressive barrier-island reservoirs with an example from the Triassic Halfway Formation, Wembley Field, Alberta, Canada. American Association of Petroleum Geologists Bulletin 78(5), 775-791.

Wright, L. D., Xu, J. P., Madsen, O. S., 1994. Across-shelf benthic transports on the inner shelf of the Middle Atlantic Bight during the “Halloween Storm” of 1991. Marine Geology 118(1-2), 61-77. DOI: 10.1016/0025-3227(94)90113-9.

Yoo, D.G., Kim, S.P., Lee, C.W., Chang, T.S., Kang, N.K., Lee, G.S., 2014. Late Quaternary inner shelf deposits in response to late Pleistocene-Holocene sea level changes: Nakdong River, SE Korea. Quaternary International 344, 156-169. DOI: 10.1016/j.quaint.2014.02.004.

Yu, L. S., Rienecker, M.M., 1999. Mechanisms for the Indian Ocean warming during the 1997-1998 El Nino. Geophysical Research Letters 26(6), 735-738. DOI: 10.1029/1999GL900072.

Yu, L. S., Rienecker, M.M., 2000: Indian Ocean warming of 1997–1998. Journal of Geophysical Research 105(C7), 16923-16939. DOI: 10.1029/2000JC900068.

Zheng, X.T., Xie, S.P., Du, Y., Liu, L., Huang, G., Liu, Q., 2013. Indian Ocean dipole response to global warming in the CMIP5 multimodel ensemble. Journal of Climate 26(16), 6067-6080.

Zong, Y., Tooley, M.J., 1999. Evidence of mid-Holocene storm-surge deposits from Morecambe Bay, northwest England: A biostratigraphical approach. Quaternary International 55(1), 43-50.

APPENDIX I

Table 3. Quantitative XRF data for Core GeoB18304-1, all values are displayed as weight percentage (wt%) at 5 cm intervals with depth down core. It should be noted that Ca and Si are interchangeable the most abundant elements present.

Core GeoB18304-1										Page 1/5
Depth Intervals	Al (wt%)	Ca (wt%)	Fe (wt%)	K (wt%)	Rb (wt%)	S (wt%)	Si (wt%)	Sr (wt%)	Ti (wt%)	Zr (wt%)
0 cm	1.5606	13.8418	0.4715	0.8681	0.0032	0.1109	19.2020	0.0793	0.1095	0.0173
5 cm	1.5377	15.0901	0.4878	0.9450	0.0037	0.1093	19.5510	0.0915	0.1141	0.0157
10 cm	1.5276	15.6396	0.4536	0.9097	0.0035	0.1047	18.9411	0.0952	0.1101	0.0184
15 cm	1.5769	14.8016	0.4973	0.9930	0.0039	0.0936	20.6859	0.0899	0.1270	0.0249
20 cm	1.3983	16.8280	0.4496	0.7950	0.0032	0.1063	17.6450	0.1015	0.1004	0.0167
25 cm	1.5318	14.9373	0.4209	0.9610	0.0036	0.1064	19.8692	0.1009	0.0892	0.0147
30 cm	1.2318	17.9690	0.4657	0.6350	0.0026	0.1229	16.9962	0.1136	0.1160	0.0234
35 cm	1.3769	17.1438	0.5281	0.6640	0.0028	0.1567	17.0061	0.1040	0.1049	0.0175
40 cm	1.0979	19.4076	0.5842	0.3663	0.0016	0.1895	14.6284	0.1319	0.1185	0.0179
45 cm	1.0891	19.3002	0.5978	0.3743	0.0018	0.1852	15.3611	0.1325	0.1091	0.0152
50 cm	1.1681	19.3913	0.6334	0.3919	0.0018	0.1998	14.5587	0.1222	0.1099	0.0191
55 cm	1.1629	17.9002	0.6338	0.3862	0.0018	0.1742	16.1689	0.1164	0.1259	0.0173
60 cm	1.0955	18.9384	0.6095	0.3706	0.0017	0.1758	15.3315	0.1256	0.1217	0.0158
65 cm	1.1703	18.3974	0.5985	0.4010	0.0017	0.1822	15.4675	0.1193	0.1076	0.0160
70 cm	1.1373	18.4765	0.6397	0.3885	0.0017	0.1757	15.9602	0.1187	0.1193	0.0153
75 cm	1.1785	17.6748	0.6175	0.3900	0.0017	0.1689	16.4056	0.1156	0.1061	0.0150
80 cm	1.1462	17.4329	0.6336	0.4051	0.0018	0.1523	17.5371	0.1169	0.1252	0.0196
85 cm	1.1491	17.8134	0.6630	0.3993	0.0019	0.1526	17.6419	0.1175	0.1286	0.0198
90 cm	1.2053	16.7498	0.6288	0.4046	0.0017	0.1572	17.1070	0.1079	0.1120	0.0191
95 cm	1.1886	16.8135	0.6401	0.4050	0.0017	0.1523	17.6825	0.1083	0.1346	0.0178

Core GeoB18304-1		Cont.								Page 2/5
Depth Intervals	Al (wt%)	Ca (wt%)	Fe (wt%)	K (wt%)	Rb (wt%)	S (wt%)	Si (wt%)	Sr (wt%)	Ti (wt%)	Zr (wt%)
100 cm	1.1731	17.7888	0.6249	0.4106	0.0018	0.1672	16.6027	0.1178	0.1107	0.0174
105 cm	1.1154	18.7819	0.6260	0.4056	0.0019	0.1646	16.7331	0.1259	0.1015	0.0146
110 cm	1.1339	17.4439	0.6131	0.4042	0.0018	0.1459	17.7997	0.1157	0.1176	0.0168
115 cm	1.1580	18.0546	0.6002	0.4042	0.0018	0.1687	16.2773	0.1198	0.1217	0.0157
120 cm	1.1556	17.8172	0.6018	0.3784	0.0017	0.1667	16.2642	0.1189	0.1139	0.0159
125 cm	1.1212	17.8998	0.6186	0.3857	0.0018	0.1568	17.1274	0.1222	0.1179	0.0138
130 cm	1.1716	17.8945	0.5998	0.4023	0.0018	0.1665	16.3160	0.1184	0.1121	0.0145
135 cm	1.1496	17.9843	0.6061	0.3947	0.0018	0.1633	16.1861	0.1233	0.1211	0.0166
140 cm	1.1495	17.8010	0.6272	0.3889	0.0017	0.1603	16.7436	0.1172	0.1264	0.0169
145 cm	1.1739	17.4567	0.6320	0.3963	0.0017	0.1583	16.9711	0.1126	0.1209	0.0170
150 cm	1.2103	17.6203	0.6324	0.3943	0.0018	0.1715	15.8975	0.1126	0.1265	0.0161
155 cm	1.1830	18.0796	0.6225	0.3992	0.0018	0.1703	15.8223	0.1128	0.1174	0.0118
160 cm	1.1436	17.6092	0.6334	0.3903	0.0018	0.1503	17.2337	0.1187	0.1368	0.0165
165 cm	1.2162	18.0845	0.6276	0.4201	0.0019	0.1763	15.9227	0.1137	0.1271	0.0134
170 cm	1.1778	17.6501	0.6321	0.4013	0.0018	0.1491	16.9683	0.1148	0.1267	0.0143
175 cm	1.1739	17.3660	0.6169	0.4155	0.0018	0.1573	17.0383	0.1131	0.1332	0.0193
180 cm	1.1699	17.5945	0.6490	0.4126	0.0017	0.1553	17.0849	0.1120	0.1249	0.0227
185 cm	1.1286	17.3144	0.6503	0.4086	0.0018	0.1345	18.2863	0.1114	0.1515	0.0209
190 cm	1.1432	17.4913	0.6330	0.4168	0.0017	0.1452	17.4497	0.1147	0.1353	0.0206
195 cm	1.1396	17.3102	0.6458	0.3896	0.0017	0.1331	17.7135	0.1082	0.1492	0.0212
200 cm	1.1296	17.6206	0.6764	0.4233	0.0017	0.1367	17.7010	0.1098	0.1599	0.0242
205 cm	1.1413	17.3680	0.6635	0.3970	0.0017	0.1411	17.7308	0.1104	0.1354	0.0214
210 cm	1.1524	17.6975	0.6704	0.4122	0.0018	0.1476	17.0801	0.1136	0.1650	0.0246
215 cm	1.1381	17.7804	0.6655	0.4281	0.0018	0.1476	17.2447	0.1159	0.1537	0.0206
220 cm	1.1254	18.6358	0.6472	0.4082	0.0017	0.1610	16.3007	0.1221	0.1566	0.0228

Core GeoB18304-1		Cont.								Page 3/5
Depth Intervals	Al (wt%)	Ca (wt%)	Fe (wt%)	K (wt%)	Rb (wt%)	S (wt%)	Si (wt%)	Sr (wt%)	Ti (wt%)	Zr (wt%)
225 cm	1.1298	17.6007	0.6372	0.4081	0.0017	0.1490	17.3693	0.1183	0.1503	0.0223
230 cm	1.1142	17.4732	0.6468	0.3806	0.0017	0.1431	17.5925	0.1148	0.1462	0.0220
235 cm	1.1664	16.9374	0.6869	0.4114	0.0018	0.1410	18.0352	0.1099	0.1752	0.0188
240 cm	1.1473	17.7006	0.6978	0.3993	0.0018	0.1409	17.5569	0.1081	0.1623	0.0269
245 cm	1.1461	17.0048	0.6818	0.4208	0.0018	0.1369	18.3198	0.1097	0.1520	0.0248
250 cm	1.1586	16.7896	0.6765	0.4087	0.0017	0.1383	18.0263	0.1046	0.1616	0.0229
255 cm	1.1441	17.6071	0.6560	0.4203	0.0018	0.1494	17.4155	0.1122	0.1569	0.0242
260 cm	1.0807	18.3120	0.7002	0.4021	0.0019	0.1453	17.5624	0.1115	0.1679	0.0244
265 cm	1.2263	17.6813	0.6671	0.5127	0.0022	0.1484	17.3738	0.1137	0.1702	0.0245
270 cm	1.2443	17.9070	0.6545	0.5303	0.0022	0.1491	16.8509	0.1110	0.1349	0.0223
275 cm	1.2312	18.2947	0.6264	0.5338	0.0023	0.1584	16.5676	0.1130	0.1583	0.0197
280 cm	1.1266	18.5714	0.6945	0.3845	0.0017	0.1574	16.1357	0.1190	0.1649	0.0312
285 cm	1.1325	18.1673	0.7081	0.4208	0.0018	0.1521	16.8829	0.1174	0.1617	0.0271
290 cm	1.1174	18.5990	0.6653	0.3687	0.0016	0.1627	16.0857	0.1221	0.1498	0.0256
295 cm	1.1230	18.3708	0.6609	0.3927	0.0018	0.1654	16.2240	0.1198	0.1473	0.0245
300 cm	1.1221	19.1128	0.6610	0.4190	0.0019	0.1630	15.5528	0.1209	0.1611	0.0266
305 cm	1.1246	18.2457	0.7261	0.3553	0.0017	0.1676	16.0463	0.1172	0.2221	0.0238
310 cm	0.9217	22.8635	0.5457	0.3248	0.0015	0.2072	12.0295	0.1578	0.1067	0.0139
315 cm	0.6808	27.3788	0.4649	0.2374	0.0013	0.2359	8.1599	0.1926	0.1077	0.0248
320 cm	1.1704	18.6907	0.6992	0.3617	0.0017	0.1847	15.6447	0.1249	0.1477	0.0224
325 cm	1.1994	18.3743	0.7289	0.3665	0.0017	0.1808	15.9707	0.1220	0.1594	0.0225
330 cm	1.0984	20.6184	0.6824	0.3390	0.0016	0.2065	13.6481	0.1370	0.1469	0.0244
335 cm	1.2558	16.8378	0.7884	0.3894	0.0017	0.1698	17.4892	0.1092	0.2215	0.0248
340 cm	1.1628	18.6709	0.7256	0.3600	0.0017	0.1862	15.2047	0.1220	0.2041	0.0376
345 cm	0.9160	23.2001	0.6239	0.3114	0.0014	0.2063	11.7873	0.1550	0.1766	0.0342

Core GeoB18304-1		Cont.								Page 4/5
Depth Intervals	Al (wt%)	Ca (wt%)	Fe (wt%)	K (wt%)	Rb (wt%)	S (wt%)	Si (wt%)	Sr (wt%)	Ti (wt%)	Zr (wt%)
350 cm	1.1762	18.6027	0.7240	0.3521	0.0015	0.1879	15.3159	0.1199	0.1799	0.0301
355 cm	1.0278	20.9844	0.6910	0.3341	0.0016	0.1919	14.2014	0.1465	0.1949	0.0307
360 cm	0.8970	21.6367	0.6507	0.2981	0.0013	0.1751	13.7011	0.1592	0.2045	0.0417
365 cm	1.2639	16.3003	0.8917	0.3960	0.0017	0.1600	18.1103	0.1008	0.2817	0.0434
370 cm	1.2686	16.2743	0.8925	0.3890	0.0017	0.1598	18.3296	0.1012	0.2992	0.0413
375 cm	1.1912	17.8224	0.8137	0.3662	0.0016	0.1625	16.6217	0.1119	0.2688	0.0393
380 cm	1.3888	14.5862	0.9947	0.4237	0.0018	0.1436	19.6611	0.0846	0.3218	0.0512
385 cm	1.3273	14.9992	0.9385	0.4086	0.0018	0.1421	19.6811	0.0900	0.3061	0.0445
390 cm	1.2647	16.3704	0.7756	0.3898	0.0018	0.1522	18.2571	0.1009	0.1900	0.0271
395 cm	1.0882	19.4557	0.7164	0.3593	0.0017	0.1670	15.5377	0.1328	0.2050	0.0387
400 cm	1.1011	19.6006	0.7091	0.3561	0.0017	0.1770	14.9782	0.1304	0.2061	0.0398
405 cm	1.1403	17.8948	0.7680	0.3740	0.0017	0.1517	17.0280	0.1193	0.2341	0.0451
410 cm	1.2815	16.0715	0.8157	0.4014	0.0018	0.1495	18.3694	0.1027	0.2456	0.0392
415 cm	1.3439	15.0568	0.9345	0.4041	0.0018	0.1489	18.9521	0.0893	0.3168	0.0548
420 cm	0.8526	23.9601	0.5005	0.3110	0.0015	0.1997	11.1431	0.1733	0.1186	0.0224
425 cm	0.9294	22.7548	0.5563	0.3417	0.0016	0.1836	11.9761	0.1543	0.1502	0.0264
430 cm	1.1925	19.4592	0.7446	0.3779	0.0018	0.1741	14.8478	0.1289	0.1995	0.0384
435 cm	1.3027	16.6730	0.8273	0.4054	0.0018	0.1440	17.7770	0.1066	0.2290	0.0378
440 cm	1.3180	16.4526	0.8377	0.3804	0.0017	0.1599	17.0750	0.1042	0.2486	0.0360
445 cm	1.2453	19.1730	0.8085	0.3981	0.0017	0.1970	14.7374	0.1283	0.2192	0.0479
450 cm	0.7450	26.5118	0.5070	0.2524	0.0013	0.2129	8.7153	0.2260	0.1251	0.0247
455 cm	0.7987	24.9933	0.5406	0.2674	0.0012	0.1926	9.9826	0.1753	0.1650	0.0324
460 cm	1.3042	17.8376	0.7847	0.4029	0.0019	0.1807	16.1480	0.1162	0.1894	0.0312
465 cm	1.4576	14.1324	0.7986	0.4539	0.0018	0.1468	19.2849	0.0870	0.2182	0.0381
470 cm	1.4388	15.3973	0.8253	0.4521	0.0019	0.1596	18.3980	0.0980	0.2240	0.0320

Core GeoB18304-1	Cont.									Page 5/5
Depth Intervals	Al (wt%)	Ca (wt%)	Fe (wt%)	K (wt%)	Rb (wt%)	S (wt%)	Si (wt%)	Sr (wt%)	Ti (wt%)	Zr (wt%)
475 cm	1.3024	16.6191	0.7146	0.4129	0.0018	0.1564	17.4082	0.1058	0.1673	0.0189
480 cm	1.4534	16.6906	0.7884	0.4395	0.0020	0.1853	16.7307	0.1093	0.1503	0.0215
485 cm	1.0108	21.3264	0.5255	0.4113	0.0017	0.1477	13.5520	0.1197	0.1390	0.0229
490 cm	1.1521	17.0377	0.5829	0.4845	0.0020	0.0944	17.8990	0.0833	0.1936	0.0324
495 cm	1.2745	14.7669	0.5886	0.5231	0.0020	0.0936	19.3549	0.0830	0.1811	0.0293
500 cm	1.1858	17.3016	0.5490	0.4989	0.0020	0.1224	17.2186	0.1072	0.1629	0.0352
505 cm	1.3757	14.7540	0.7652	0.4955	0.0019	0.1113	19.5922	0.0926	0.2202	0.0386
510 cm	1.3536	13.2282	0.7329	0.5009	0.0019	0.0958	21.1211	0.0768	0.2444	0.0444

Table 4. Quantitative XRF data for Core GeoB18303-2, all values are displayed as weight percentage (wt%) at 5 cm intervals with depth down core. It should be noted that Ca and Si are interchangeable the most abundant elements present.

Core GeoB18303-2										Page 1/5
Depth Intervals	Al (wt%)	Ca (wt%)	Fe (wt%)	K (wt%)	Rb (wt%)	S (wt%)	Si (wt%)	Sr (wt%)	Ti (wt%)	Zr (wt%)
5 cm	1.8847	12.9310	1.0633	0.6035	0.0025	0.1547	20.5314	0.0841	0.2551	0.0409
10 cm	1.6758	17.0284	1.0663	0.5430	0.0024	0.1806	16.8640	0.1156	0.2861	0.0509
15 cm	1.3527	22.5296	0.9125	0.4392	0.0020	0.2259	10.8966	0.1663	0.2489	0.0540
20 cm	1.4260	21.6730	0.9684	0.4759	0.0022	0.2245	12.6426	0.1621	0.2670	0.0500
25 cm	1.2888	22.8290	0.8734	0.4283	0.0019	0.2268	11.1610	0.1647	0.2600	0.0508
30 cm	1.2581	22.8760	0.8678	0.4486	0.0021	0.2136	11.6760	0.1726	0.2328	0.0523
35 cm	1.2648	22.6732	0.8946	0.4365	0.0021	0.1981	11.8535	0.1786	0.2533	0.0533
40 cm	1.2994	22.9166	0.9018	0.4559	0.0020	0.2115	11.5698	0.1831	0.2692	0.0584

Core GeoB18303-2 Cont. Page 2/5

Depth Intervals	Al (wt%)	Ca (wt%)	Fe (wt%)	K (wt%)	Rb (wt%)	S (wt%)	Si (wt%)	Sr (wt%)	Ti (wt%)	Zr (wt%)
45 cm	1.2419	23.2300	0.8907	0.4448	0.0022	0.2095	11.3274	0.1737	0.2730	0.0608
50 cm	1.2382	23.3793	0.8848	0.4413	0.0021	0.2065	11.5157	0.1685	0.2665	0.0530
55 cm	1.2569	23.3091	0.9619	0.4374	0.0020	0.1966	11.6696	0.1587	0.2979	0.0667
60 cm	1.2192	23.6328	0.8838	0.4159	0.0020	0.2112	10.9552	0.1707	0.2782	0.0526
65 cm	1.2451	23.6011	0.8627	0.4661	0.0021	0.2045	10.9980	0.1590	0.2485	0.0556
70 cm	1.1128	24.9586	0.8020	0.4545	0.0020	0.2038	9.9799	0.1895	0.2701	0.0638
75 cm	1.2267	24.3918	0.8977	0.4423	0.0021	0.2048	10.5009	0.1945	0.2342	0.0515
80 cm	1.1388	23.9612	0.8705	0.4165	0.0019	0.1958	10.7852	0.1784	0.2497	0.0574
85 cm	1.0915	24.2547	0.8691	0.4417	0.0018	0.1929	10.7594	0.1618	0.2846	0.0657
90 cm	1.1162	24.0565	0.8763	0.3989	0.0018	0.1896	10.9609	0.1748	0.2887	0.0711
95 cm	1.0890	24.8612	0.8794	0.4536	0.0019	0.1862	10.3943	0.1571	0.3024	0.0746
100 cm	1.1264	24.2910	0.8574	0.4920	0.0022	0.1967	10.5327	0.1678	0.2969	0.0677
105 cm	1.1725	23.1207	0.9817	0.4185	0.0019	0.1959	11.5692	0.1549	0.3447	0.0814
110 cm	1.3069	22.7944	1.0682	0.4541	0.0019	0.2022	11.6379	0.1532	0.3879	0.0832
115 cm	1.1202	23.8998	0.9373	0.4246	0.0019	0.1936	11.1728	0.1518	0.3324	0.0829
120 cm	1.1088	23.9167	0.8361	0.4187	0.0020	0.1834	10.7511	0.1647	0.2849	0.0603
125 cm	1.2780	21.8404	0.9687	0.4154	0.0018	0.1893	12.0370	0.1459	0.3113	0.0682
130 cm	1.5190	17.4834	1.1852	0.4811	0.0020	0.1634	16.8713	0.1221	0.3762	0.0758
135 cm	1.3539	19.2144	1.2535	0.4153	0.0018	0.1500	15.8111	0.1407	0.4523	0.1052
140 cm	1.6765	14.6602	1.1226	0.5027	0.0021	0.1761	19.2211	0.0997	0.3384	0.0582
145 cm	0.8474	28.1366	0.4716	0.4392	0.0019	0.1979	7.0677	0.1817	0.1220	0.0256
150 cm	0.6885	30.6204	0.4698	0.2838	0.0015	0.2159	5.1799	0.3785	0.1441	0.0308
155 cm	0.8439	28.1198	0.5863	0.3265	0.0016	0.2096	6.9530	0.1991	0.1403	0.0329
160 cm	0.5941	31.4234	0.3837	0.2793	0.0014	0.2143	4.8851	0.2264	0.0844	0.0190
165 cm	0.6619	30.1162	0.4090	0.2851	0.0014	0.2124	5.8167	0.2567	0.0997	0.0210

Core GeoB18303-2	Cont.									Page 3/5
Depth Intervals	Al (wt%)	Ca (wt%)	Fe (wt%)	K (wt%)	Rb (wt%)	S (wt%)	Si (wt%)	Sr (wt%)	Ti (wt%)	Zr (wt%)
170 cm	0.7685	29.8819	0.5391	0.3258	0.0017	0.2170	5.6260	0.2015	0.1065	0.0238
175 cm	0.7598	29.6276	0.4396	0.3718	0.0016	0.2119	5.8840	0.2241	0.0986	0.0202
180 cm	0.6983	30.2084	0.4188	0.3037	0.0016	0.2357	5.3174	0.2406	0.0908	0.0204
185 cm	1.2113	25.3149	0.6152	0.5788	0.0026	0.2750	9.9123	0.1709	0.1209	0.0226
190 cm	2.6343	16.7345	1.1423	1.1268	0.0050	0.3879	16.4380	0.1084	0.2101	0.0418
195 cm	4.1569	10.3756	2.0151	1.5974	0.0072	0.8086	20.4915	0.0751	0.3188	0.0397
200 cm	0.7758	29.4942	0.3460	0.4201	0.0019	0.2872	6.0933	0.1988	0.0816	0.0169
205 cm	0.7499	30.1259	0.3608	0.3745	0.0019	0.2860	5.6734	0.2034	0.0801	0.0138
210 cm	0.7758	29.6004	0.4091	0.4222	0.0020	0.2973	5.9806	0.2145	0.0864	0.0218
215 cm	0.8190	28.6245	0.3766	0.4300	0.0020	0.2709	6.7099	0.1945	0.0808	0.0182
220 cm	0.6947	29.8738	0.4071	0.3243	0.0016	0.2902	5.9452	0.2534	0.0938	0.0149
225 cm	1.7302	23.4196	0.8260	0.7740	0.0037	0.3808	11.1309	0.1745	0.1564	0.0247
230 cm	0.7365	29.8160	0.3546	0.4122	0.0019	0.2709	6.0013	0.2095	0.0825	0.0145
235 cm	0.7010	29.6234	0.3749	0.3654	0.0017	0.2812	6.0653	0.2078	0.0785	0.0171
240 cm	0.7651	28.7814	0.3527	0.4353	0.0020	0.2662	6.6450	0.2026	0.0804	0.0160
245 cm	0.7538	29.0019	0.3723	0.4076	0.0019	0.2561	6.8843	0.2145	0.0837	0.0203
250 cm	0.7404	29.5451	0.3579	0.4120	0.0020	0.2746	6.2743	0.2366	0.0893	0.0164
255 cm	0.7645	28.9885	0.3667	0.4255	0.0019	0.2730	6.3693	0.2043	0.0898	0.0180
260 cm	0.7619	29.5634	0.3769	0.4039	0.0020	0.2948	6.3516	0.2026	0.0941	0.0168
265 cm	0.7747	29.0692	0.3635	0.4389	0.0046	0.2708	6.6358	0.2028	0.0894	0.0144
270 cm	0.8513	28.0996	0.3709	0.4858	0.0023	0.2688	7.0619	0.1886	0.0830	0.0150
275 cm	0.7966	28.5534	0.4894	0.4173	0.0018	0.3091	6.7094	0.1979	0.0781	0.0131
280 cm	0.7510	29.0616	0.3395	0.4063	0.0019	0.2641	6.5517	0.2287	0.0848	0.0130
285 cm	0.7752	28.3798	0.3331	0.4359	0.0019	0.2437	7.0879	0.1843	0.0770	0.0124
290 cm	0.6828	30.1522	0.2775	0.3894	0.0019	0.2642	5.7132	0.2114	0.0606	0.0105

Core GeoB18303-2	Cont.									Page 4/5
Depth Intervals	Al (wt%)	Ca (wt%)	Fe (wt%)	K (wt%)	Rb (wt%)	S (wt%)	Si (wt%)	Sr (wt%)	Ti (wt%)	Zr (wt%)
295 cm	0.7167	29.4411	0.2767	0.4266	0.0021	0.2287	6.4476	0.2672	0.0560	0.0109
300 cm	1.0764	24.5161	0.3264	0.6223	0.0029	0.2159	10.1600	0.1895	0.0587	0.0082
305 cm	0.8050	27.9926	0.2309	0.5142	0.0022	0.1982	7.7799	0.2044	0.0432	0.0077
310 cm	0.7364	29.6282	0.2158	0.5296	0.0024	0.2381	6.1957	0.2022	0.0415	0.0099
315 cm	0.8941	27.2189	0.3253	0.5330	0.0023	0.2419	8.2928	0.1618	0.0706	0.0120
320 cm	0.8131	27.4025	0.2293	0.5059	0.0023	0.2268	8.1422	0.1662	0.0409	0.0074
325 cm	1.1029	23.8920	0.2859	0.6565	0.0028	0.2275	10.7583	0.1292	0.0634	0.0089
330 cm	0.9216	26.1031	0.2378	0.6184	0.0026	0.2108	8.9413	0.1447	0.0446	0.0088
335 cm	1.0661	24.2812	0.2590	0.6679	0.0029	0.2104	10.6887	0.1301	0.0453	0.0066
340 cm	1.0323	24.9482	0.2634	0.6209	0.0027	0.2357	9.7134	0.1293	0.0472	0.0075
345 cm	0.9588	26.6509	0.2502	0.6193	0.0027	0.2364	8.3752	0.1442	0.0439	0.0080
350 cm	1.0191	25.0435	0.2595	0.6221	0.0027	0.2293	9.7232	0.1323	0.0498	0.0085
355 cm	1.0723	24.5007	0.2719	0.6799	0.0030	0.2352	10.2645	0.1309	0.0449	0.0080
360 cm	1.1696	22.9956	0.2823	0.7397	0.0032	0.2165	11.6164	0.1215	0.0572	0.0094
365 cm	1.0918	24.5685	0.2991	0.6261	0.0026	0.2519	9.6442	0.1330	0.0540	0.0074
370 cm	1.1967	22.6665	0.3046	0.7187	0.0030	0.2247	11.6126	0.1140	0.0548	0.0068
375 cm	0.9725	26.7310	0.2760	0.5931	0.0025	0.2436	7.9842	0.1494	0.0538	0.0128
380 cm	0.9246	26.3694	0.2364	0.5910	0.0026	0.2296	8.6076	0.1463	0.0460	0.0073
385 cm	1.0406	24.9966	0.2814	0.6189	0.0028	0.2415	9.5779	0.1473	0.0516	0.0101
390 cm	1.1143	23.7172	0.2659	0.7152	0.0031	0.2271	10.9788	0.1211	0.0475	0.0090
395 cm	1.0625	25.1048	0.2724	0.6687	0.0030	0.2408	9.5856	0.1249	0.0491	0.0076
400 cm	1.1743	23.6572	0.2827	0.7548	0.0031	0.2283	10.8997	0.1191	0.0487	0.0074
405 cm	1.2079	22.4550	0.2915	0.7559	0.0032	0.2260	11.9656	0.1120	0.0506	0.0097
410 cm	1.1546	23.8700	0.2591	0.7547	0.0031	0.2210	11.2101	0.1240	0.0424	0.0063
415 cm	1.2406	22.7661	0.2782	0.7903	0.0034	0.2352	11.5811	0.1127	0.0559	0.0092

Core GeoB18303-2	Cont.									Page 5/5
Depth Intervals	Al (wt%)	Ca (wt%)	Fe (wt%)	K (wt%)	Rb (wt%)	S (wt%)	Si (wt%)	Sr (wt%)	Ti (wt%)	Zr (wt%)
420 cm	0.9535	26.9384	0.2494	0.6143	0.0028	0.2512	8.2140	0.1473	0.0423	0.0067
425 cm	1.1737	23.6417	0.3198	0.7522	0.0033	0.2541	10.9554	0.1170	0.0548	0.0077
430 cm	0.9370	26.5649	0.2244	0.6497	0.0029	0.2376	8.6963	0.1558	0.0398	0.0075
435 cm	1.1497	23.5316	0.3064	0.7354	0.0031	0.2407	10.8805	0.1231	0.0576	0.0071
440 cm	0.9961	26.6094	0.2524	0.6843	0.0030	0.2462	8.6360	0.1423	0.0469	0.0062
445 cm	1.1679	23.8249	0.3220	0.7252	0.0032	0.2669	10.2222	0.1201	0.0552	0.0125
450 cm	1.0904	24.5324	0.3050	0.7000	0.0029	0.2569	9.9193	0.1386	0.0563	0.0078
455 cm	1.2410	23.8800	0.3428	0.7997	0.0034	0.2628	10.6144	0.1291	0.0585	0.0084
460 cm	1.5273	20.9084	0.4264	0.9771	0.0040	0.2467	12.8146	0.1185	0.0813	0.0095
465 cm	1.6215	20.5229	0.4353	1.0999	0.0043	0.2555	13.1232	0.1069	0.1039	0.0124
470 cm	1.5071	22.0562	0.5183	0.9590	0.0040	0.2901	12.1776	0.1055	0.1019	0.0135
475 cm	1.4134	20.0984	0.3976	0.9398	0.0034	0.2390	14.3086	0.1022	0.0699	0.0099
480 cm	1.6604	21.0083	0.5245	1.1032	0.0044	0.3119	12.9088	0.1118	0.1059	0.0160
485 cm	1.5542	22.3948	0.7633	0.8413	0.0035	0.3581	11.1344	0.1288	0.1928	0.0213
490 cm	2.7305	9.9481	1.0583	1.0536	0.0038	0.4330	22.1381	0.0536	0.1758	0.0147
495 cm	2.5648	8.4964	1.0647	1.1098	0.0039	0.4005	25.0761	0.0456	0.1767	0.0132

Table 5. Quantitative XRD data for Core GeoB18304-1, a total of 14 samples were from horizons indicated with depth down core. All values are displayed as weight percentage (wt%). It should be noted that Quartz (Qtz) and Carbonate mineral concentration are the most abundant elements present in the distal core.

Core GeoB18304-1						
Depth interval (cm)	Qtz (wt%)	Plag (wt%)	K-feld (wt%)	Carbonates (wt%)	Phyllosilicates (wt%)	Comments and trace minerals
30	45.0223	8.4061	14.6576	19.1248	11.4101	Hematite
40	43.5787	4.7422	7.8573	28.9986	13.8386	Corundum
150	45.6979	4.1206	4.6789	35.0554	9.5850	Corundum
310	30.2840	9.7799	7.0133	38.4617	11.7572	Hematite1:1 Ilmenite, Anhydrite, Nepheline, Marcasite
315	34.1796	4.0646	2.1594	49.8948	8.5094	Corundum, Rutile
320	45.4494	8.3382	14.4259	22.3795	9.0212	
335	53.7090	7.4295	3.5819	21.8313	11.4031	Corundum, Zoisite (Epidote)
360	41.8498	7.7329	4.3799	34.3997	9.8193	
385	58.5542	5.3267	3.6352	23.3917	9.2074	
420	45.2591	4.8992	4.0476	33.3570	11.9253	Corundum
450	40.0511	4.5588	2.4183	42.3530	6.3146	Corundum, Rutile, Phyrhotite
470	54.4138	6.8742	5.8781	18.0337	14.4980	
485	55.8446	4.4078	5.6284	24.8097	8.2129	Corundum, Hematite
500	60.7988	8.1768	3.1053	17.2732	8.6913	Hematite

Table 6. Quantitative XRD data for Core GeoB18303-2, where a total of seven samples were taken from all values are displayed as weight percentage (wt%) sampled at selected horizons with depth down core. It should be noted that Quartz (Qtz) and Carbonate mineral concentration are the most abundant elements present in the proximal core.

Core GeoB18303-2						
Depth interval (cm)	Qtz (wt%)	Plag (wt%)	K-feld (wt%)	Carbonates (wt%)	Phyllosillicates (wt%)	Comments and trace minerals
140	50.4053	6.6375	5.1567	25.3859	11.7354	ZnO
160	16.3208	10.1484	12.0857	54.6590	4.1954	
195	34.0156	14.6696	13.4817	22.6458	10.4576	Gypsum, Epistilbite (Zeolite)
210	21.5553	3.1673	6.5242	59.0437	8.0163	
225	27.1999	9.1862	17.6520	30.1841	11.1979	Hematite 4:1 Limmonite, Marcasite, Gypsum, Talc
305	22.9806	7.5182	13.8744	41.7562	12.1373	Corundum
495	46.5365	13.2292	16.3806	6.2598	14.2008	Hematite, Stilbite (Zeolite)

Appendix II

Table 7. Grainsize data for core GeoB18304-1 sampled at 5 cm depth intervals. All grain size values for both the clastic and bulk sediment component are displayed as phi values. In comparison with the bulk sediment component it is evident that the clastic sediment is significantly finer with higher phi values displayed.

Core GeoB18304-1		Page 1/3
Depth intervals (cm)	Grain size (phi)	
	Clastic sediment	Bulk sediment
0	0.8560	0.6946
5	0.8588	0.5118
10	0.9799	0.6155
15	0.9094	0.5461
20	0.9931	0.5454
25	0.9624	0.7415
30	1.1338	0.4298
35	2.0795	1.0156
40	2.1798	1.6142
45	2.1649	1.6181
50	2.1930	1.6963
55	2.1890	1.6611
60	2.1884	1.4634
65	2.0850	1.4786
70	1.9165	1.5233
75	2.1514	1.5385
80	2.1115	1.7128
85	2.1668	1.7742
90	2.1507	1.6412
95	2.1266	1.7602
100	2.1552	1.8229
105	2.2183	1.6538
110	2.2163	1.7078
115	2.2122	1.6657
120	2.2365	1.6104
125	2.1811	1.6551
130	2.1636	1.6479
135	2.1740	1.6330
140	2.1805	1.6215
145	2.1636	1.6017
150		1.6538
155	2.2076	1.6671

Core GeoB18303-2	Cont.	Page 2/3
Depth intervals (cm)	Grain size (phi)	
	Clastic sediment	Bulk sediment
160	2.0203	1.5551
165	1.9896	1.5851
170	2.1272	1.5722
175	2.1329	1.6713
180	2.1022	1.6140
185		1.5074
190	2.1128	1.6641
195	2.1297	1.5659
200	2.1247	1.5297
205	2.1078	1.5399
210	2.0541	1.5828
215	2.0813	1.4407
220	2.0589	1.6087
225	2.0954	1.5124
230	2.0831	1.4865
235	2.1097	1.5135
240	2.1329	1.6178
245	2.9828	1.5642
250	2.0831	1.6447
255	2.1041	1.6173
260	2.1109	1.4832
265	1.9965	1.5671
270	2.1507	1.5958
275	1.8599	1.6203
280	1.8344	1.7418
285	2.0905	1.3883
290	2.1450	1.4943
295	2.1234	0.9538
300	2.7869	1.5223
305	2.9324	1.8842
310	3.0979	0.6996
315	2.7720	0.6208
320	2.7179	1.9276
325	2.8489	1.5496
330	2.7879	2.0239
335	2.7859	1.9353
340	2.8130	1.4985
345	3.2056	1.3212

Core GeoB18303-2		Cont. Page 3/3
Depth intervals (cm)	Grain size (phi)	
	Clastic sediment	Bulk sediment
350	2.3364	1.7394
355	2.8283	0.8107
360	2.6074	1.3100
365	2.5303	1.9629
370	2.6538	2.2130
375	2.7084	2.1826
380	2.6385	2.2098
385	2.8900	1.5984
390	2.5547	2.1271
395	2.9236	1.6258
400	2.3982	1.1065
405	2.4430	1.4281
410	1.9771	2.1246
415	1.9948	1.0193
420	2.4204	1.4841
425	2.4787	1.6506
430	2.5278	2.2750
435	2.5838	0.9985
440	2.6906	1.8172
445	2.3226	0.6330
450	2.7112	1.1185
455	2.5838	2.1736
460	2.6584	2.3094
465	2.6242	2.3629
470	2.8293	2.2100
475	2.2723	2.0291
480	1.6790	-0.0607
485	2.0967	1.2216
490	2.9247	1.6445
495	2.6730	1.9445
500	2.3974	

Table 8. Grainsize data for core GeoB18303-2 sampled at 5 cm depth intervals. All grain size values for both the clastic and bulk sediment component are displayed as phi values. In comparison with the bulk sediment component it is evident that the clastic sediment is significantly finer with higher phi values displayed. When compared to core GeoB18304-1 it is evident that the more distal core is composed of coarser material with lower grain size phi values for the clastic and bulk sediment component.

Core GeoB18303-2		Page 1/3
Depth intervals (cm)	Grain size (phi)	
	Clastic sediment	Bulk sediment
5	2.8314	1.8900
10	2.7789	1.3233
15	2.9324	0.7695
20	3.0493	0.7228
25	2.9148	0.7143
30	2.7293	0.3662
35	3.0093	0.4586
40		0.3038
45	2.8826	0.3613
50	3.0942	0.8355
55	2.9512	0.9278
60	2.9324	0.3309
65	3.0856	0.5840
70	2.7302	0.4482
75	2.7602	1.0900
80	2.8922	1.0401
85	2.6776	1.0784
90	2.7179	1.0847
95	2.7037	0.5035
100	3.1304	0.6744
105	2.3437	0.9910
110	2.4422	0.5636
115	2.3459	0.7197
120	2.4066	0.1681
125	2.5295	0.8144
130	2.4868	0.3587
135	2.7141	1.2642
140	2.6657	1.5893
145	2.2345	1.1722
150		0.0397
155	2.3255	-0.0835
160	2.3778	-0.2433
165	2.4957	-0.2829

Core GeoB18303-2		Cont. Page 2
Depth intervals (cm)	Grain size (phi)	
	Clastic sediment	Bulk sediment
170	2.4643	-0.2024
175	2.2009	0.1869
180	1.9241	-0.0642
185	3.2709	0.3993
190	3.4283	1.6298
195	1.9051	2.6957
200	1.4150	0.4402
205	1.5370	-0.1627
210	1.7198	-0.0566
215	1.5522	-0.2837
220	1.4812	-0.1296
225	3.5474	-0.3978
230	1.5274	1.9981
235	1.6210	-0.4868
240	1.3511	-0.3110
245	1.4864	-0.1080
250	1.5245	-0.2804
255	1.4800	-0.1812
260	1.5577	-0.1453
265	1.3812	-0.3631
270	1.7515	-0.3225
275	1.7269	-0.3514
280	1.3051	-0.2584
285	1.5208	-0.5546
290	1.2553	-0.3192
295	1.3383	-0.3854
300		-0.0487
305	0.9851	-0.1441
310	0.5370	-0.6603
315	1.0297	0.1231
320	0.9917	-0.1569
325	1.0162	0.0515
330	1.0309	0.1608
335	0.7013	0.2154
340	0.8362	0.3500
345	0.5853	0.3348
350	0.9343	0.4787
355	0.8419	0.6529

Core GeoB18303-2		Cont. Page 3/3
Depth intervals (cm)	Grain size (phi)	
	Clastic sediment	Bulk sediment
360	0.7524	0.5462
365	0.9957	0.4211
370	0.8520	0.6016
375	0.6739	0.2594
380	0.7683	-0.0344
385	1.0481	0.0204
390	1.1209	0.4745
395	0.9086	0.1889
400	0.7745	0.0666
405	0.8746	0.4265
410	0.6647	0.3931
415	0.6407	0.1144
420	0.6936	0.1237
425	0.8143	0.1026
430	0.6391	0.1033
435	0.6131	-0.0095
440	1.1623	0.1040
445	0.9610	0.5113
450		0.2921
455	1.5526	-0.5957
460	0.7615	0.0527
465	0.6534	-0.2096
470		0.1502
475	0.5090	0.1479
480	0.7200	0.3405
485	0.6235	1.8833
490	2.7293	2.0148
495	3.3553	